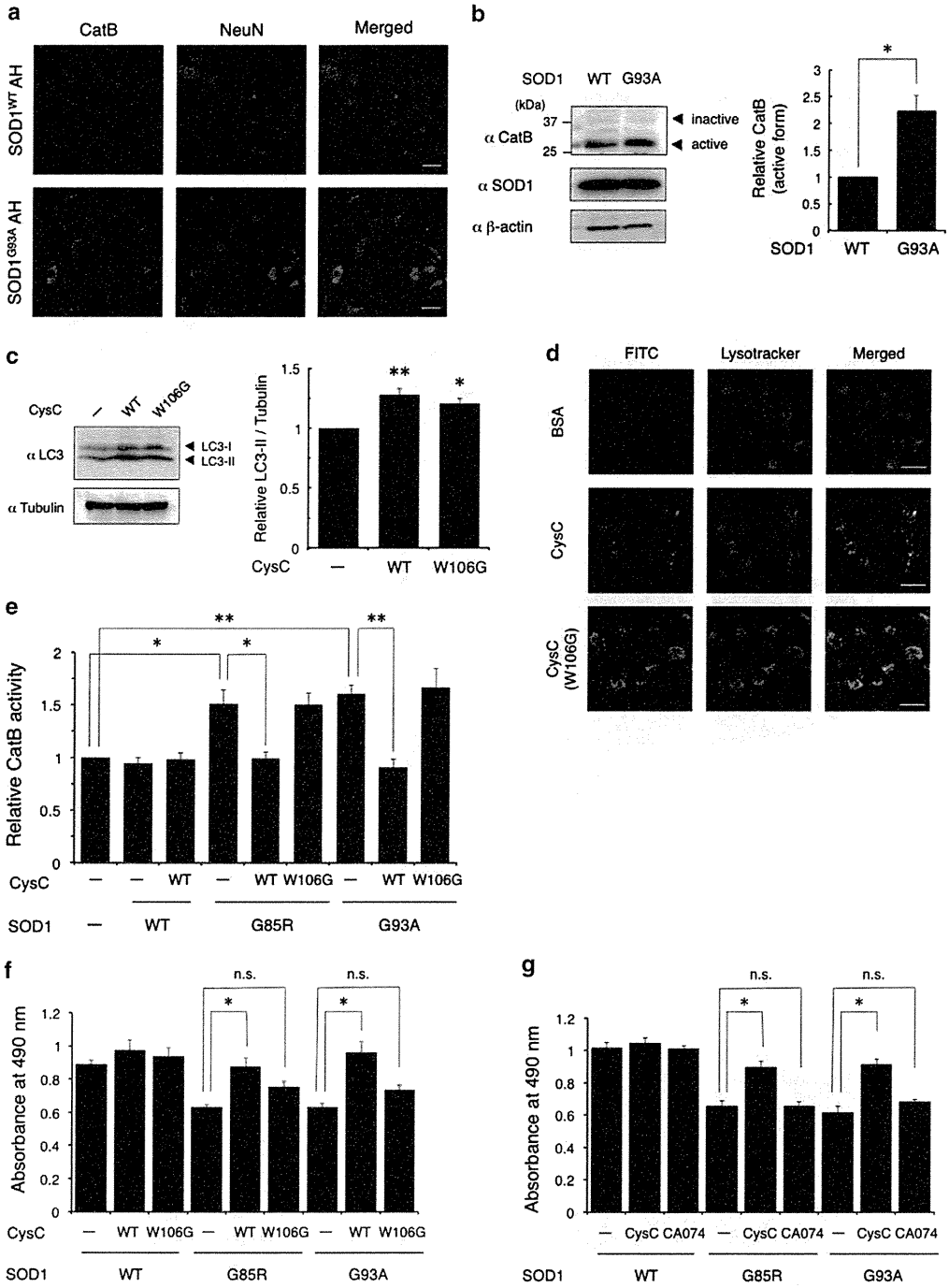

Figure 7 Transduced CysC exerts neuroprotective activity through the inhibition of Cathepsin B. (**a**) Expression of CatB in mouse spinal cords. Transverse sections in anterior horn (AH) of $SOD1^{WT}$ or $SOD1^{G93A}$ 5-month-old mouse spinal cords were analyzed by confocal microscopy. Scale bar: 50 μm (**b**) Induction of active form CatB in the $SOD1^{G93A}$ mouse spinal cord. Lysates of $SOD1^{WT}$ or $SOD1^{G93A}$ 5-month-old mouse spinal cords were analyzed by immunoblotting. Quantification of CatB relative to β-actin in immunoblots (bottom). (**c**) Induction of autophagy by wild-type (WT) or W106G CysC. N2a cells were treated with CysC (0.6 μM) for 24 h. The lysates of the cells were analyzed by immunoblotting. (**d**) Intracellular transduction of WT and W106G CysC. N2a cells were treated with FITC-CysC (1 μM) for 3 h and observed by confocal microscopy. Scale bar: 25 μm (**e**) Enzymatic activities of CatB were measured by the luciferase assay with a CatB-specific substrate. N2a cells transiently expressing mutant SOD1 species were treated with CysC (1 μM) for 24 h. The lysates of the cells were used for measuring CatB activity. (**f** and **g**) Protective effects of WT and W106G CysC (**f**), and a CatB-specific inhibitor CA-074 (**g**). The viability of N2a cells was examined by the MTS assay after incubation for 48 h in the differentiation medium with WT or W106G CysC (0.2 μM), or CA-074 methyl ester (10 μM). These experiments were independently performed three times with triplicate samples. All data were shown as means $\pm$ S.E.M. $^{**}P<0.01$. $^{*}P<0.05$

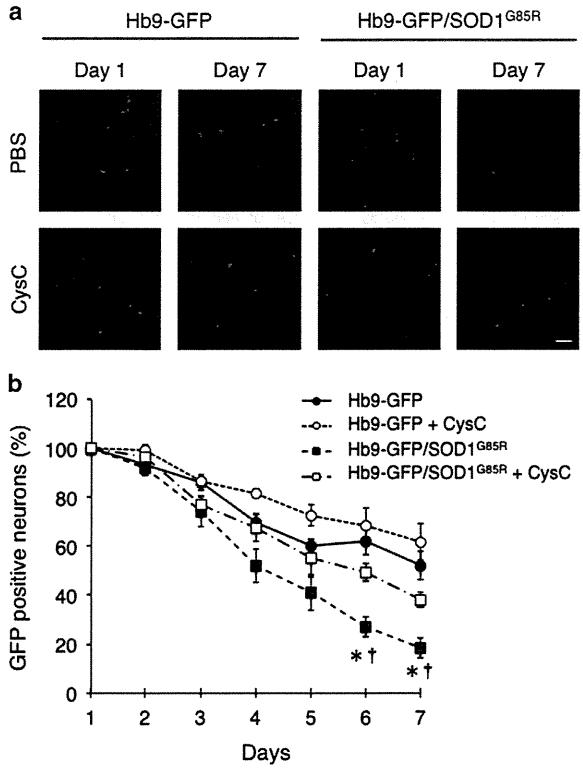

Figure 8 CysC protects primary cultured motor neurons *in vitro*. (**a**) Representative fluorescent images of the primary spinal cord mix culture from Hb9-GFP or Hb9-GFP/SOD1^{G85R} transgenic mouse embryos. The spinal mix culture was treated with or without CysC. GFP-positive cells represent motor neurons. Scale bar: 100 μm. (**b**) The viability of motor neurons in the spinal cord mix culture of Hb9-GFP (closed circle, solid line), Hb9-GFP with CysC (open circle, dotted line), Hb9-GFP/SOD1^{G85R} (closed square, broken line) and Hb9-GFP/SOD1^{G85R} with CysC (open square, dashed line). GFP-positive motor neurons were quantified. Data are expressed as means $\pm$ S.E.M. from three independent experiments. The cells were counted in nine random fields in each experiment ($n=3$). *$P<0.05$ compared to Hb9-GFP without CysC. †$P<0.01$ compared to Hb9-GFP/SOD1^{G85R} with CysC

CysC protected neuronal cells through two distinct pathways: (i) induction of autophagy through AMPK activation and (ii) inhibition of aberrantly activated CatB. Furthermore, the coordinated activation of these two pathways was required for neuroprotection by CysC.

Autophagy is a major degradation pathway of misfolded or unfolded proteins as well as the ubiquitin-proteasomal pathway[41] and regulation of basal autophagy is crucial for neural survivals.[42,43] Impairment of the ubiquitin-proteasomal pathway, which has been reported in both SOD1-related[17,18] and SOD1-unrelated[19,20] ALS models implies that activation of the autophagy pathway may complementally contribute to degradation of abnormal toxic proteins. Indeed, inducers of autophagy such as progesterone, trehalose or rapamycin showed neuroprotective effects by degrading toxic species.[21,22,29,44] Our finding that CysC induces autophagy to protect neurons is consistent with these previous results. Reduction of the intracellular aggregates (Figure 3a) and the Triton-insoluble mutant SOD1 protein (Figure 3d) suggested induction of autophagic protein degradation by CysC. Furthermore, 3-MA treatment demonstrated that induction of autophagy is essential for the neuroprotective activity of CysC (Figure 3c). As induction of autophagy by CysC also protects neurons against various stresses other than SOD1-mediated toxicity[16] and rapamycin protected neurons in mice expressing TAR DNA binding protein 43 (TDP-43), another disease-linked protein accumulated in sporadic ALS and frontotemporal lobar degeneration,[22] CysC treatment may also be useful for SOD1-unrelated ALS as well as the SOD1-linked one. Although autophagy is generally considered as a neuroprotective pathway, autophagy inducers are not effective[45] or can even exacerbate the disease progression.[46] We demonstrated that induction of autophagy is essential for neuroprotection by CysC (Figure 3c). However, induction of autophagy by AICAR treatment (Figures 4d and e) or W106G CysC mutant (Figures 7c and f) alone was insufficient to protect neuronal cells against the mutant SOD1-mediated toxicity. These data suggest that activation of multiple neuroprotective pathways including autophagy is required for neuroprotection. In addition to this, it has recently been suggested that these inconsistent results might be due to the side effects of rapamycin, which are independent of autophagy induction.[47] In light of this, CysC-mediated autophagy is one of the neuroprotective mechanisms against mutant SOD1-mediated neurotoxicity and may be a promising candidate for neuroprotection.

We demonstrated that CysC activated AMPK to inhibit mTOR (Figure 4). AMPK was inactivated both in the *in vitro* and *in vivo* models of SOD1-linked ALS, suggesting that metabolic aberration is involved in the disease and that CysC possibly contributes to restore intracellular metabolic homeostasis. Moreover, inducing autophagy by CysC through AMPK activation even without mutant SOD1 implies the idea that CysC is a regulator of basal autophagy required for neuronal survival. However, in a previous study, the reduced activity of AMPK improved the motor activity of neurons in *C. elegans* without halting neurodegeneration.[48] Their findings seem to be in contradiction to our findings. One possible interpretation is that coordinated activation of AMPK is required to inhibit neurodegeneration. As we demonstrated, AMPK inhibition by CC prevented the neuroprotection by CysC (Figure 4e), indicating AMPK activation is essential. On the other hand, we also showed that AMPK-specific activation by AICAR exacerbated the mutant SOD1-mediated toxicity (Figure 4e), which is consistent with a previous study,[48] and CatB inhibitory activity of CysC is also required for neuroprotection (Figure 7). These data indicate that AMPK-specific activation is not sufficient to protect the neuronal cells and, eventually, might be toxic. Therefore, we suggest that the synergetic regulation of intracellular signaling pathways should be required for neuroprotection.

Aberrant CatB activation is correlated with motor neuronal death in sporadic ALS cases[23] and the SOD1^{G93A} mice model.[24] We showed that inhibition of CatB activity by CysC was also essential for its neuroprotective activity (Figure 7), supporting the idea that aberrant proteolysis mediated by CatB is highly toxic to motor neurons. It should be noted that the W106G CysC mutant did not rescue the cells at all (Figure 7f), regardless of its ability for intracellular transduction

and autophagy induction. Moreover, CatB-specific inhibition by CA-074 was also not protective (Figure 7g). These results suggest that autophagy is less protective alone and synergistic activation of multiple neuroprotective pathways is crucial to ameliorate neurodegeneration in ALS.

Interestingly, transduced CysC inhibited CatB only when CatB was activated by stress without affecting basal CatB activity, suggesting that the transduced CysC was inactivated in the lysosomes and reactivated under stress conditions. As CysC forms a reversible dimer and/or oligomer under low pH conditions *in vitro*[49] and dimeric CysC does not inhibit CatB,[50] acidic condition in the lysosomes might contribute to this stress-inducible response of CysC. CysC was leaked into cytosol only when mutant SOD1 species were expressed (Figure 6), supporting this notion. Moreover, involvement of lysosomal dysfunction in neurodegeneration, especially LMP and LMP-caused lysosomal proteinase leakage possibly including CatB, is also implicated by our data (Figures 1d and 6) and previous studies.[37,38] Therefore, CysC released from lysosome by LMP may specifically inhibit aberrant cytosolic proteolysis caused by leaked CatB.

CysC was transduced into N2a cells and localized to lysosomes, which was like that seen in the other cell lines[32,33] through clathrin-dependent endocytosis (Figure 5). We also revealed that transduced CysC leaked into the cytosol from the lysosomes and aggregated oxidative stress-dependently (Figures 6b and c). These data suggest that stress-induced CysC release from the lysosomes is a first step in forming Bunina bodies. However, Bunina bodies are not found in familial ALS patients with SOD1 mutations.[26,27] One possible interpretation is that the amount of CysC in neurons is not enough to form Bunina bodies in those SOD1-linked ALS cases. Indeed, the immunoreactivity of CysC in SOD1^{G93A} mouse spinal cord was apparently reduced (Figure 1). In addition to this, increased CysC immunoreactivity in non-neuronal cells (Figure 1c) implies dysfunction of the CysC secretory pathway. Therefore, the downregulation of CysC level in the neurons carrying SOD1 mutations may inhibit the formation of Bunina bodies. Further studies are required to investigate the mechanism of Bunina bodies' formation.

We demonstrate here that CysC, a main component of Bunina bodies in ALS, is an endogenous neuroprotective factor that acts through coordinated activation of two distinct neuroprotective pathways: induction of autophagy and inhibition of aberrant CatB activity. We expect further investigations of the mechanisms through which CysC accumulates and maintains proteostasis in motor neurons should clarify the role of Bunina bodies in ALS. Furthermore, targeting CysC in motor neurons may become a novel therapeutic strategy for ALS.

Materials and Methods

Antibodies. Antibodies against phosphorylated PKCδ (Thr507), AMPKα 1/2 (Thr172) and anti- LAMP-2 antibody were obtained from Santa Cruz Biotechnology Inc. (Santa Cruz, CA, USA). The anti-phosphorylated mammalian target of rapamycin (mTOR) (Ser2448) antibody was obtained from Cell Signaling Technology Inc. (Danvers, MA, USA). Antibodies against NeuN, CatB and CysC were obtained from EMD Millipore Corp. (Billerica, MA, USA). Alexa Fluor-conjugated secondary antibodies were purchased from Life Technologies Corp. (Grand Island, NY, USA). We also used the following commercially available antibodies: anti-c-myc (Roche, Basel, Switzerland), anti-tubulin, anti-β-actin (both from Sigma-Aldrich Co. LLC St. Louis, MO, USA) and anti-LC3 (Novus Biologicals LLC, Littleton, CO, USA). Rabbit anti-human SOD1 was raised in our laboratory against a recombinant human SOD1 peptide (24–36) and purified with protein A.[51]

Transgenic mice. Wild-type, mutant SOD1 (B6.Cg-Tg(SOD1-G37R) 1Dwc/J), (B6.Cg-Tg(SOD1-G85R) 148Dwc/J), (B6.Cg-Tg(SOD1-G93A) 1Gur/J) and Hb9-GFP (B6.Cg-Tg(Hlxb9-GFP) 1Tmj/J) transgenic mice were obtained from the Jackson Laboratory (Bar Harbor, ME, USA) or were gifts from Dr. Don Cleveland (University of California, San Diego). The mice were genotyped by polymerase chain reactions with the following sense and antisense primers: 5′-CATC AGCCCTAATCCATCTGA-3′, 5′-CGCGACTAACAATCAAAGTGA-3′, respectively. The mice were housed and treated in compliance with the requirements of the Animal Care and Use Committee of RIKEN Brain Science Institute and Nagoya University.

Immunofluorescence staining. Immunofluorescence staining was performed as described previously.[52] In brief, after blocking, the sections were incubated with anti-CysC (1 : 100), anti-Cathepsin B, anti-NeuN (1 : 500) and/or anti-LAMP-2 (1 : 100) overnight at 4 °C. Bound antibodies were detected with Alexa Fluor 488-conjugated anti-rabbit IgG, Alexa Fluor 594-conjugated anti-mouse IgG and Alexa Fluor 650-conjugated anti-rat IgG antibodies (all 1 : 1000). Immunostained images were obtained by confocal laser scanning microscopy (LSM 5 Exciter, LSM-700; Carl Zeiss AG, Oberkochen, Germany) and the equipped software (Zen; Carl Zeiss AG).

Construction, expression and purification of recombinant human CysC protein. The DNA fragment containing human CysC (lacking the 26 amino acids leader sequence of the precursor CysC) was amplified by polymerase chain reactions and cloned into the pET-20b(+) vector (EMD Millipore) under *pelB* signal sequence for potential periplasmic localization. Overexpression of CysC was induced in *Escherichia coli* strain Rosetta (DE3) (EMD Millipore) by treatment with 0.3 mM isopropyl-β-D-thiogalactopylanoside for 4.5 h at 30 °C and CysC protein was purified according to the osmotic shock protocol (EMD Millipore) to prepare for periplasmic fraction with some modifications.[53,54] In brief, the cells were resuspended in an equal volume of 30 mM Tris-HCl (pH 9.0), 20% (w/w) sucrose. Then, ethylenediaminetetraacetic acid was added to 1 mM. The cells were agitated for 10 min at room temperature and centrifuged at 13 000 × *g* for 10 min. The pellet was resuspended in an equal volume of ice-cold 10 mM Tris-HCl (pH 9.0) and 5 mM $MgSO_4$, then it was agitated for 10 min at 4 °C. The cell debris was removed by centrifugation at 13 000 × *g* for 10 min at 4 °C and the supernatant was loaded onto a DEAE sepharose anion-exchange column equilibrated with 50 mM Tris-HCl (pH 9.0). The flow-through was collected and concentrated. Purified CysC was dialyzed against 10 mM Tris-HCl (pH 9.0) and 150 mM NaCl. Endotoxin was removed from the protein solutions by phase separation using Triton-X 114 (Wako Pure Chemical Industries Ltd., Osaka, Japan).[55,56] The amounts of Triton X-114 were removed by ultrafiltration with an Amicon Ultra centrifugal unit (EMD Millipore). The protein concentration of CysC was determined spectrophotometrically with an extinction coefficient of 11.5 mM/cm at 280 nm.[57]

Biotin or FITC labeling of CysC proteins. CysC was conjugated to D-biotin, succinimidyl azide (Life Technologies) or FITC (Dojindo Laboratories, Kumamoto, Japan) according to the manufacturers' instructions. Labeled CysC was purified with G25 gel chromatography to eliminate any unconjugated reagents. The conjugation of biotin to CysC was confirmed by an immunoblotting assay using horseradish peroxidase conjugated streptavidin (Thermo Fisher Scientific Inc., Waltham, MA, USA). The concentrations of CysC protein and FITC dye were calculated on the basis of their absorbance at 280 and 494 nm, respectively. The molar ratio of dye per protein was determined to be 0.9–1.8.

Cell culture. N2a cells were maintained in Dulbecco's modified Eagle's medium (DMEM) containing 4.5 g/l glucose supplemented with 10% (v/v) fetal bovine serum (FBS), 100 U/ml penicillin and 100 μg/ml streptomycin (all from Life Technologies) in a humidified atmosphere containing 5% CO_2 at 37 °C. To differentiate the cells, the cells were cultured with a differentiation medium (DMEM containing 4.5 g/l glucose supplemented with 2% (v/v) FBS and 2 mM N,N-dibutyladenosine 3′,5′-phosphoric acid (dbcAMP; Nacalai Tesque Inc., Kyoto, Japan)).

Isolation of intact lysosomes from Neuro2a cells. Lysosomes were isolated by an Optiprep (Axis-Shield plc, Dundee, UK) gradient centrifugation as previously reported.[58,59] Briefly, the cells treated with 1 μM Biotin-CysC for 24 h were homogenized in 10 mM HEPES-KOH (pH 7.4), 0.25 M sucrose and 1 mM ethylenediamineteraacetic acid with a Potter-Elehjem tissue grinder (Wheaton, Millville, NJ, USA). The cell debris and nuclei were removed by centrifugation at 600 × *g* for 5 min at 4 °C. The post-nuclear fraction was further centrifuged at 3000 × *g* for 10 min at 4 °C to remove the mitochondrial fraction. The resultant supernatant was loaded onto an Optiprep gradient (1 ml each of 10, 12, 14, 16 and 18% (w/v)) and centrifuged at 145 000 × *g* for 2 h at 4 °C. One milliliter from the top was collected and analyzed by immunoblotting.

Immunoblotting. N2a cells seeded at 2.0×10^5 cells/ml in 6-well plates were transfected with pcDNA3.3-SOD1 expression vectors by Lipofectamine 2000 (Life Technologies). After 24 h of incubation, the medium was replaced with the differentiation medium with CysC, rapamycin (EMD Millipore, 300 nM) or E64d/Pepstatin A (both from Sigma, 10 mg/ml each). After the indicated time of incubation at 37 °C, the cells were washed with ice-cold phosphate-buffered saline (PBS) twice and harvested in TNE lysis buffer (50 mM Tris-HCl (pH 7.4), 150 mM NaCl, 1 mM ethylenediamineteraacetic acid, 1% Triton-X 100, protease inhibitor cocktail and PhosSTOP (both from Roche)). The cells or spinal cord lysates of the transgenic mice in TNE lysis buffer were sonicated and centrifuged at 15 000 × *g* for 5 min at 4 °C. The protein concentrations in the supernatants were measured by micro BCA assay kit (Thermo Fisher Scientific Inc.). Each 15 μg/lane of total proteins was analyzed by immunoblotting. Densitometric analysis was performed after the chemiluminescence detection by using an image analyzer LAS-4000mini (Fuji film, Tokyo, Japan) with the equipped software (Multi Gauge: Fuji film).

Neurotoxicity assays. Neurotoxicity was analyzed as previously reported[60] with slight modifications. N2a cells were seeded at 5.0×10^4 cells/ml in poly-D-lysine coated 96-well plates in DMEM containing 1.0 g/l glucose supplemented with 10% (v/v) FBS. After transfection, the cells were differentiated for 48 h in DMEM containing 1.0 g/l glucose supplemented with 2% (v/v) FBS and 2 mM dbcAMP with or without CysC, 3-methyladenine (3-MA; Sigma), CC (EMD Millipore), AICA-riboside (AICAR; EMD Millipore) or CA-074 methyl ester (EMD Millipore). The number of live cells was manually counted by trypan blue staining or estimated by CellTiter 96 AQueous One Solution Cell Proliferation Assay kit (Promega Biosciences, San Louis Obispo, CA, USA) containing MTS as described by the manufacturer. A primary glia-neuron mix culture was prepared from E12.5 embryonic spinal cord of Hb9-GFP/SOD1^{G85R} mouse. The cells were maintained in DMEM supplemented with 10% (v/v) FBS and the medium was changed every 3 days. The numbers of GFP-positive motor neuronal cells were counted manually with fluorescent microscopy.

Examination of CysC transduction into cells with fluorescence microscopy. N2a cells were seeded at 1.0×10^5 cells/ml in poly-D-lysine-coated 35 mm glass-bottomed dishes (MatTek Corp., Ashford, MA, USA). The medium was replaced with the differentiation medium containing 1 μM FITC-CysC or 300 nM rapamycin at 6 h after the transfection of pcDNA3.3-SOD1 or pAcGFP-N1-SOD1. The cells were further incubated for 24 h. To determine the CysC endocytotic pathway, the cells were treated with 25 μM chlorpromazine (Wako), 5 mg/ml filipin III (Enzo Life Sciences Inc., Farmingdale, NY, USA) or 25 μM 5-(N-Ethyl-N-isopropyl) amiloride (Enzo) for 1 h. The medium was replaced with the differentiation one with or without 1 μM FITC-CysC and incubated for another 1 h. The cells were stained with Lysotracker-Red (Life Technologies) according to the manufacturer's instructions to visualize the lysosomal acidic components. The cells were washed with PBS twice and observed by confocal laser scanning microscopy.

CatB activity assay. N2a cells were seeded at 2.0×10^5 cells/ml in 60 mm dishes and transfected with pcDNA3.3-SOD1 expression vectors by Lipofectamine 2000. After 24 h of transfection, the medium was replaced with differentiation medium containing 1 μM wild-type or W106G CysC. The cells were incubated for 24 h at 37 °C in 5% CO_2 and harvested in ice-cold PBS. Intracellular CatB activities were measured with a Cathepsin B Activity Assay kit (BioVision Inc., Mountain View, CA, USA) as described in the manufacturer's protocol.

Statistics. Neuroprotective activity of CysC on primary cultured motor neurons was analyzed by a two-way ANOVA with subsequent post hoc *t*-tests. All other quantified data were analyzed by a one-way ANOVA with subsequent post hoc *t*-tests or by a Student's *t*-test.

Conflict of Interest

The authors declare no conflict of interest.

Acknowledgements. This work was funded by Grants-in-Aid for Scientific Research 23111006 (to KY), 23117704 (to KW), 25860252 (to SW) from the Ministry for Education, Culture and Sports, Science and Technology, Japan, Grant-in-Aid for Research on Rare and Intractable Diseases, the Research Committee on Establishment of Novel Treatments for Amyotrophic Lateral Sclerosis, from the Ministry of Health, Labour and Welfare of Japan, and Japan Science Technology, CREST. We thank the members of the Laboratory for Motor Neuron Disease and the Support Unit for Biomaterial Analysis in RIKEN BSI Research Resource Center for the DNA analyses.

1. Cleveland DW, Rothstein JD. From Charcot to Lou Gehrig: deciphering selective motor neuron death in ALS. *Nat Rev Neurosci* 2001; **2**: 806–819.
2. Bendotti C, Carri MT. Lessons from models of SOD1-linked familial ALS. *Trends Mol Med* 2004; **10**: 393–400.
3. Bruijn LI, Miller TM, Cleveland DW. Unraveling the mechanisms involved in motor neuron degeneration in ALS. *Annu Rev Neurosci* 2004; **27**: 723–749.
4. Watanabe M, Dykes-Hoberg M, Culotta VC, Price DL, Wong PC, Rothstein JD. Histological evidence of protein aggregation in mutant SOD1 transgenic mice and in amyotrophic lateral sclerosis neural tissues. *Neurobiol Dis* 2001; **8**: 933–941.
5. Valentine JS, Hart PJ. Misfolded CuZnSOD and amyotrophic lateral sclerosis. *Proc Natl Acad Sci USA* 2003; **100**: 3617–3622.
6. Gruzman A, Wood WL, Alpert E, Prasad MD, Miller RG, Rothstein JD *et al.* Common molecular signature in SOD1 for both sporadic and familial amyotrophic lateral sclerosis. *Proc Natl Acad Sci USA* 2007; **104**: 12524–12529.
7. Guareschi S, Cova E, Cereda C, Ceroni M, Donetti E, Bosco DA *et al.* An over-oxidized form of superoxide dismutase found in sporadic amyotrophic lateral sclerosis with bulbar onset shares a toxic mechanism with mutant SOD1. *Proc Natl Acad Sci USA* 2012; **109**: 5074–5079.
8. Abrahamson M, Barrett AJ, Salvesen G, Grubb A. Isolation of six cysteine proteinase inhibitors from human urine. Their physicochemical and enzyme kinetic properties and concentrations in biological fluids. *J Biol Chem* 1986; **261**: 11282–11289.
9. Hochwald GM, Pepe AJ, Thorbecke GJ. Trace proteins in biological fluids. IV. Physicochemical properties and sites of formation of gamma-trace and beta-trace proteins. *Proc Soc Exp Biol Med* 1967; **124**: 961–966.
10. Gauthier S, Kaur G, Mi W, Tizon B, Levy E. Protective mechanisms by cystatin C in neurodegenerative diseases. *Front Biosci* 2011; **3**: 541–554.
11. Mi W, Pawlik M, Sastre M, Jung SS, Radvinsky DS, Klein AM *et al.* Cystatin C inhibits amyloid-beta deposition in Alzheimer's disease mouse models. *Nat Genet* 2007; **39**: 1440–1442.
12. Xu L, Sheng J, Tang Z, Wu X, Yu Y, Guo H *et al.* Cystatin C prevents degeneration of rat nigral dopaminergic neurons: in vitro and in vivo studies. *Neurobiol Dis* 2005; **18**: 152–165.
13. Okamoto K, Hirai S, Amari M, Watanabe M, Sakurai A. Bunina bodies in amyotrophic lateral sclerosis immunostained with rabbit anti-cystatin C serum. *Neurosci Lett* 1993; **162**: 125–128.
14. Tsuji-Akimoto S, Yabe I, Niino M, Kikuchi S, Sasaki H. Cystatin C in cerebrospinal fluid as a biomarker of ALS. *Neurosci Lett* 2009; **452**: 52–55.
15. Wilson ME, Boumaza I, Lacomis D, Bowser R. Cystatin C: a candidate biomarker for amyotrophic lateral sclerosis. *PLoS One* 2010; **5**: e15133.
16. Tizon B, Sahoo S, Yu H, Gauthier S, Kumar AR, Mohan P *et al.* Induction of autophagy by cystatin C: a mechanism that protects murine primary cortical neurons and neuronal cell lines. *PLoS One* 2010; **5**: e9819.
17. Hyun DH, Lee M, Halliwell B, Jenner P. Proteasomal inhibition causes the formation of protein aggregates containing a wide range of proteins, including nitrated proteins. *J Neurochem* 2003; **86**: 363–373.
18. Urushitani M, Kurisu J, Tsukita K, Takahashi R. Proteasomal inhibition by misfolded mutant superoxide dismutase 1 induces selective motor neuron death in familial amyotrophic lateral sclerosis. *J Neurochem* 2002; **83**: 1030–1042.
19. Watanabe S, Kaneko K, Yamanaka K. Accelerated disease onset with stabilized familial amyotrophic lateral sclerosis (ALS)-linked mutant TDP-43 proteins. *J Biol Chem* 2013; **288**: 3641–3654.
20. Tashiro Y, Urushitani M, Inoue H, Koike M, Uchiyama Y, Komatsu M *et al.* Motor neuron-specific disruption of proteasomes, but not autophagy, replicates amyotrophic lateral sclerosis. *J Biol Chem* 2012; **287**: 42984–42994.
21. Kim J, Kim TY, Cho KS, Kim HN, Koh JY. Autophagy activation and neuroprotection by progesterone in the G93A-SOD1 transgenic mouse model of amyotrophic lateral sclerosis. *Neurobiol Dis* 2013; **59**: 80–85.
22. Wang IF, Guo BS, Liu YC, Wu CC, Yang CH, Tsai KJ *et al.* Autophagy activators rescue and alleviate pathogenesis of a mouse model with proteinopathies of the TAR DNA-binding protein 43. *Proc Natl Acad Sci USA* 2012; **109**: 15024–15029.

23. Kikuchi H, Yamada T, Furuya H, Doh-ura K, Ohyagi Y, Iwaki T *et al.* Involvement of cathepsin B in the motor neuron degeneration of amyotrophic lateral sclerosis. *Acta Neuropathol* 2003; **105**: 462–468.
24. Wootz H, Weber E, Korhonen L, Lindholm D. Altered distribution and levels of cathepsinD and cystatins in amyotrophic lateral sclerosis transgenic mice: possible roles in motor neuron survival. *Neuroscience* 2006; **143**: 419–430.
25. Sun L, Wu Z, Baba M, Peters C, Uchiyama Y, Nakanishi H. Cathepsin B-dependent motor neuron death after nerve injury in the adult mouse. *Biochem Biophys Res Commun* 2010; **399**: 391–395.
26. Hirano A. Neuropathology of ALS: an overview. *Neurology* 1996; **47**(4 Suppl 2): S63–S66.
27. Hirano A, Kurland LT, Sayre GP. Familial amyotrophic lateral sclerosis. A subgroup characterized by posterior and spinocerebellar tract involvement and hyaline inclusions in the anterior horn cells. *Arch Neurol* 1967; **16**: 232–243.
28. Kim J, Kundu M, Viollet B, Guan KL. AMPK and mTOR regulate autophagy through direct phosphorylation of Ulk1. *Nat Cell Biol* 2011; **13**: 132–141.
29. Nave BT, Ouwens M, Withers DJ, Alessi DR, Shepherd PR. Mammalian target of rapamycin is a direct target for protein kinase B: identification of a convergence point for opposing effects of insulin and amino-acid deficiency on protein translation. *Biochem J* 1999; **344**(Pt 2): 427–431.
30. Dave KR, Raval AP, Purroy J, Kirkinezos IG, Moraes CT, Bradley WG *et al.* Aberrant deltaPKC activation in the spinal cord of Wobbler mouse: a model of motor neuron disease. *Neurobiol Dis* 2005; **18**: 126–133.
31. Ozpolat B, Akar U, Mehta K, Lopez-Berestein G. PKC delta and tissue transglutaminase are novel inhibitors of autophagy in pancreatic cancer cells. *Autophagy* 2007; **3**: 480–483.
32. Ekstrom U, Wallin H, Lorenzo J, Holmqvist B, Abrahamson M, Aviles FX. Internalization of cystatin C in human cell lines. *FEBS J* 2008; **275**: 4571–4582.
33. Wallin H, Abrahamson M, Ekstrom U. Cystatin C properties crucial for uptake and inhibition of intracellular target enzymes. *J Biol Chem* 2013; **288**: 17019–17029.
34. Munch C, O'Brien J, Bertolotti A. Prion-like propagation of mutant superoxide dismutase-1 misfolding in neuronal cells. *Proc Natl Acad Sci USA* 2011; **108**: 3548–3553.
35. Ros-Baro A, Lopez-Iglesias C, Peiro S, Bellido D, Palacin M, Zorzano A *et al.* Lipid rafts are required for GLUT4 internalization in adipose cells. *Proc Natl Acad Sci USA* 2001; **98**: 12050–12055.
36. Kabayama H, Takeuchi M, Taniguchi M, Tokushige N, Kozaki S, Mizutani A *et al.* Syntaxin 1B suppresses macropinocytosis and semaphorin 3A-induced growth cone collapse. *J Neurosci* 2011; **31**: 7357–7364.
37. Kurz T, Terman A, Gustafsson B, Brunk UT. Lysosomes and oxidative stress in aging and apoptosis. *Biochim Biophys Acta* 2008; **1780**: 1291–1303.
38. Yamashima T, Oikawa S. The role of lysosomal rupture in neuronal death. *Prog Neurobiol* 2009; **89**: 343–358.
39. Mason RW, Sol-Church K, Abrahamson M. Amino acid substitutions in the N-terminal segment of cystatin C create selective protein inhibitors of lysosomal cysteine proteinases. *Biochem J* 1998; **330**(Pt 2): 833–838.
40. Wichterle H, Lieberam I, Porter JA, Jessell TM. Directed differentiation of embryonic stem cells into motor neurons. *Cell* 2002; **110**: 385–397.
41. Klionsky DJ, Emr SD. Autophagy as a regulated pathway of cellular degradation. *Science* 2000; **290**: 1717–1721.
42. Komatsu M, Waguri S, Chiba T, Murata S, Iwata J, Tanida I *et al.* Loss of autophagy in the central nervous system causes neurodegeneration in mice. *Nature* 2006; **441**: 880–884.
43. Hara T, Nakamura K, Matsui M, Yamamoto A, Nakahara Y, Suzuki-Migishima R *et al.* Suppression of basal autophagy in neural cells causes neurodegenerative disease in mice. *Nature* 2006; **441**: 885–889.
44. Castillo K, Nassif M, Valenzuela V, Rojas F, Matus S, Mercado G *et al.* Trehalose delays the progression of amyotrophic lateral sclerosis by enhancing autophagy in motoneurons. *Autophagy* 2013; **9**: 1308–1320.
45. Pizzasegola C, Caron I, Daleno C, Ronchi A, Minoia C, Carri MT *et al.* Treatment with lithium carbonate does not improve disease progression in two different strains of SOD1 mutant mice. *Amyotroph Lateral Scler* 2009; **10**: 221–228.
46. Zhang X, Li L, Chen S, Yang D, Wang Y, Zhang X *et al.* Rapamycin treatment augments motor neuron degeneration in SOD1(G93A) mouse model of amyotrophic lateral sclerosis. *Autophagy* 2011; **7**: 412–425.
47. Staats KA, Hernandez S, Schonefeldt S, Bento-Abreu A, Dooley J, Van Damme P *et al.* Rapamycin increases survival in ALS mice lacking mature lymphocytes. *Mol Neurodegener* 2013; **8**: 31.
48. Lim MA, Selak MA, Xiang Z, Krainc D, Neve RL, Kraemer BC *et al.* Reduced activity of AMP-activated protein kinase protects against genetic models of motor neuron disease. *J Neurosci* 2012; **32**: 1123–1141.
49. Ekiel I, Abrahamson M. Folding-related dimerization of human cystatin C. *J Biol Chem* 1996; **271**: 1314–1321.
50. Merz GS, Benedikz E, Schwenk V, Johansen TE, Vogel LK, Rushbrook JI *et al.* Human cystatin C forms an inactive dimer during intracellular trafficking in transfected CHO cells. *J Cell Physiol* 1997; **173**: 423–432.
51. Bruijn LI, Becher MW, Lee MK, Anderson KL, Jenkins NA, Copeland NG *et al.* ALS-linked SOD1 mutant G85R mediates damage to astrocytes and promotes rapidly progressive disease with SOD1-containing inclusions. *Neuron* 1997; **18**: 327–338.
52. Yamashita H, Kawamata J, Okawa K, Kanki R, Nakamizo T, Hatayama T *et al.* Heat-shock protein 105 interacts with and suppresses aggregation of mutant Cu/Zn superoxide dismutase: clues to a possible strategy for treating ALS. *J Neurochem* 2007; **102**: 1497–1505.
53. Abrahamson M, Dalboge H, Olafsson I, Carlsen S, Grubb A. Efficient production of native, biologically active human cystatin C by Escherichia coli. *FEBS Lett* 1988; **236**: 14–18.
54. Dalboge H, Jensen EB, Tottrup H, Grubb A, Abrahamson M, Olafsson I *et al.* High-level expression of active human cystatin C in Escherichia coli. *Gene* 1989; **79**: 325–332.
55. Aida Y, Pabst MJ. Removal of endotoxin from protein solutions by phase separation using Triton X-114. *J Immunol Methods* 1990; **132**: 191–195.
56. Liu S, Tobias R, McClure S, Styba G, Shi Q, Jackowski G. Removal of endotoxin from recombinant protein preparations. *Clin Biochem* 1997; **30**: 455–463.
57. Gill SC, von Hippel PH. Calculation of protein extinction coefficients from amino acid sequence data. *Anal Biochem* 1989; **182**: 319–326.
58. Sevlever D, Jiang P, Yen SH. Cathepsin D is the main lysosomal enzyme involved in the degradation of alpha-synuclein and generation of its carboxy-terminally truncated species. *Biochemistry* 2008; **47**: 9678–9687.
59. Wei J, Fujita M, Nakai M, Waragai M, Sekigawa A, Sugama S *et al.* Protective role of endogenous gangliosides for lysosomal pathology in a cellular model of synucleinopathies. *Am J Pathol* 2009; **174**: 1891–1909.
60. Niwa J, Yamada S, Ishigaki S, Sone J, Takahashi M, Katsuno M *et al.* Disulfide bond mediates aggregation, toxicity, and ubiquitylation of familial amyotrophic lateral sclerosis-linked mutant SOD1. *J Biol Chem* 2007; **282**: 28087–28095.

BMJ Open

Differential motor neuron involvement in progressive muscular atrophy: a comparative study with amyotrophic lateral sclerosis

Yuichi Riku,[1] Naoki Atsuta,[1] Mari Yoshida,[2] Shinsui Tatsumi,[2] Yasushi Iwasaki,[2] Maya Mimuro,[2] Hirohisa Watanabe,[1] Mizuki Ito,[1] Jo Senda,[1] Ryoichi Nakamura,[1] Haruki Koike,[1] Gen Sobue[1]

To cite: Riku Y, Atsuta N, Yoshida M, *et al*. Differential motor neuron involvement in progressive muscular atrophy: a comparative study with amyotrophic lateral sclerosis. *BMJ Open* 2014;**4**: e005213. doi:10.1136/bmjopen-2014-005213

► Prepublication history and additional material is available. To view please visit the journal (http://dx.doi.org/10.1136/bmjopen-2014-005213).

YR and NA contributed equally.

Received 7 March 2014
Revised 7 April 2014
Accepted 10 April 2014

[1]Department of Neurology, Nagoya University Graduate School of Medicine, Nagoya, Japan
[2]Institute for Medical Science of Aging, Aichi Medical University, Aichi, Japan

Correspondence to
Dr Gen Sobue;
sobueg@med.nagoya-u.ac.jp

ABSTRACT

Objective: Progressive muscular atrophy (PMA) is a clinical diagnosis characterised by progressive lower motor neuron (LMN) symptoms/signs with sporadic adult onset. It is unclear whether PMA is simply a clinical phenotype of amyotrophic lateral sclerosis (ALS) in which upper motor neuron (UMN) signs are undetectable. To elucidate the clinicopathological features of patients with clinically diagnosed PMA, we studied consecutive autopsied cases.

Design: Retrospective, observational.

Setting: Autopsied patients.

Participants: We compared clinicopathological profiles of clinically diagnosed PMA and ALS using 107 consecutive autopsied patients. For clinical analysis, 14 and 103 patients were included in clinical PMA and ALS groups, respectively. For neuropathological evaluation, 13 patients with clinical PMA and 29 patients with clinical ALS were included.

Primary outcome measures: Clinical features, UMN and LMN degeneration, axonal density in the corticospinal tract (CST) and immunohistochemical profiles.

Results: Clinically, no significant difference between the prognosis of clinical PMA and ALS groups was shown. Neuropathologically, 84.6% of patients with clinical PMA displayed UMN and LMN degeneration. In the remaining 15.4% of patients with clinical PMA, neuropathological parameters that we defined as UMN degeneration were all negative or in the normal range. In contrast, all patients with clinical ALS displayed a combination of UMN and LMN system degeneration. CST axon densities were diverse in the clinical PMA group, ranging from low values to the normal range, but consistently lower in the clinical ALS group. Immunohistochemically, 85% of patients with clinical PMA displayed 43-kDa TAR DNA-binding protein (TDP-43) pathology, while 15% displayed fused-in-sarcoma (FUS)-positive basophilic inclusion bodies. All of the patients with clinical ALS displayed TDP-43 pathology.

Conclusions: PMA has three neuropathological background patterns. A combination of UMN and LMN degeneration with TDP-43 pathology, consistent with ALS, is the major pathological profile. The remaining patterns have LMN degeneration with TDP-43 pathology without UMN degeneration, or a combination of UMN and LMN degeneration with FUS-positive basophilic inclusion body disease.

Strengths and limitations of this study

- The characteristics of motor neuron involvement in amyotrophic lateral sclerosis or progressive muscular atrophy were comprihensively described.
- The severity of upper motor neuron involvement was semiquantitatively compared between the clinical groups, and quantitatively surrogated by axonal densities in the corticospinal tract.
- Pathological results clearly indicated the differences of upper motor neuron involvement between the clinical groups.
- To evaluate the entire regions in the motor cortex or the corticospinal tract is not possible.
- We prepared formalin-fixed, paraffin-embedded tissues to quantificate axonal densities in the corticospinal tract. In this protocol, the tissues can be distorted compared with the conventional fixation using glutaraldehyde and Epon. The results can vary more than those from other histological techniques.

INTRODUCTION

Motor neuron disease (MND) constitutes a group of heterogeneous neurodegenerative diseases that are associated with progressive upper motor neuron (UMN) and/or lower motor neuron (LMN) degeneration. A portion of MND cases has genetic causes; however, the majority of MND cases are sporadic and of unknown aetiology. Amyotrophic lateral sclerosis (ALS) constitutes the majority of MND cases. ALS is a clinicopathological disorder that presents with progressive UMN and LMN symptoms/signs. Neuropathologically,

the UMN and LMN systems exhibit neuronal loss and gliosis and Bunina bodies are detected in surviving neurons. Although various immunohistochemical profiles have been identified in patients with ALS, 43-kDa TAR DNA-binding protein (TDP-43) is the major pathological protein in sporadic ALS.[1]

In contrast, MND that presents with LMN symptoms/signs alone occurs in several disorders, including genetically mediated disorders such as, spinal muscular atrophy (SMA), symmetrical axonal neuropathy and spinal and bulbar muscular atrophy (SBMA).[2 3] Additionally, a sporadic and adult-onset LMN disease has been referred to as progressive muscular atrophy (PMA).[3 4] Although the revised El Escorial criteria, the standard diagnostic criteria for ALS, exclude patients who only present with LMN symptoms/signs, several studies have revealed that a subset of patients with clinically diagnosed PMA exhibit the neuropathological hallmarks of ALS. Postmortem histopathological studies have revealed corticospinal tract (CST) degeneration in more than half of the patients with MND clinically limited to LMN symptoms/signs.[5 6] TDP-43-immunoreactive inclusions have been detected in the LMNs and cortical neurons of patients with PMA.[7 8] The disease course of PMA is relentlessly progressive, although somewhat longer than that of ALS.[2 4 9 10]

However, it is unclear whether clinically diagnosed PMA is simply a clinical phenotype of ALS in which UMN symptoms/signs are undetectable. In this study, we investigated the clinicopathological profiles of patients with clinically diagnosed PMA compared with those of patients with clinically diagnosed ALS using a series of consecutive adult-onset sporadic MND autopsy cases.

METHODS

Patients and clinical evaluations

We enrolled 130 consecutive autopsied patients who were clinically diagnosed with and pathologically confirmed as suffering from sporadic, adult-onset MND at the Department of Neuropathology of the Institute for Medical Science of Aging at the Aichi Medical University from January 1998 to December 2010. All of the patients had been clinically evaluated by neurological experts at the Nagoya University Hospital, the Aichi Medical University Hospital or their affiliated hospitals. Permission to perform an autopsy and archive the brain and spinal cord for research purposes was obtained from the patients' relatives by the attending physician after death. We evaluated the clinical profiles of the included patients by retrospectively reviewing case notes written at the time of diagnosis and in an advanced disease stage. Disease onset was defined as the time at which patients became aware of muscle weakness. The inclusion criteria for the patients with MND were as follows: older than 18 years at disease onset; no family history of ALS, PMA, progressive lateral sclerosis, inherited SMA or SBMA or any other neurodegenerative disorder; motor neuron involvement based on neurological examination and neuropathological evidence of neuronal loss and gliosis in the UMN and/or LMN systems that were not due to any cerebrovascular diseases, metabolic disorders, genetic neurological disorders, inflammatory disorders, neoplasms or traumas. We excluded 22 patients due to invalid clinical data and 1 patient with only UMN symptoms/signs throughout his disease course; 107 patients were ultimately included in this study. Based on the clinical data, we separated these 107 patients with MND into two groups, namely the clinical PMA and clinical ALS groups. According to a previous study,[4] clinical PMA was defined by neurological evidence of LMN involvement (decreased or diminished deep tendon reflexes and muscle atrophy) and a lack of UMN symptoms/signs (increased jaw jerk, other exaggerated tendon reflexes, Babinski sign, other pathological reflexes, forced crying and forced laughing) throughout the clinical course. Patients who exhibited motor conduction block(s) based on extensive standardised nerve conduction studies,[11] exhibited objective sensory signs (apart from mild vibration sensory disturbances in elderly patients) or had a history of diseases that may mimic MND (eg, spinal radiculopathy, poliomyelitis and diabetic amyotrophy) were not included in the clinical PMA group.[4] We defined clinical ALS, based on the revised El Escorial criteria, as fulfilling 'possible' or above categories, which require UMN signs/symptoms in at least one region of the body.[12]

Pathological evaluations

For pathological evaluations, we excluded one patient with clinical PMA due to severe anoxic changes in the brain and four patients with clinical ALS due to insufficient tissue material. Ultimately, we enrolled 13 patients with clinical PMA for pathological evaluations. For comparison, we enrolled 29 patients with clinical ALS who were consecutively autopsied during the past 5 years of the study period (after January 2006). Additionally, 13 age-matched controls (mean age at death 68 ±6.91 years) were enrolled. We prepared 8 mm coronal sections of the cerebrum and 5 mm axial sections of the brainstem. The tissues were fixed using 20% neutral-buffered formalin, embedded in paraffin and sectioned at a thickness of 4.5 μm. We evaluated the sections from the precentral gyrus (four segments from the left hemisphere), hippocampus, brainstem and spinal cord. In all cases, the spinal cord was examined at all segment levels. Two investigators (YR and MY) evaluated the degeneration of the motor neuron systems and the immunohistochemical profiles of the included patients. The investigators were completely blinded to each patient's ID and the clinical diagnosis corresponding to each specimen. With respect to the degeneration of motor neuron systems, the severity of motor neuron loss in the primary motor cortex, facial and hypoglossal nuclei and spinal anterior horns, myelin pallor within the CST and aggregation of macrophages within the

primary motor cortex and CST were evaluated. The evaluations were performed on the most severely affected lesions and graded as none (−), mild (+), moderate (++) or severe (+++; figure 1). The immunohistochemical profiles were evaluated using anti-pTDP-43 and antifused-in-sarcoma (FUS) antibodies in the LMN system and cerebrum. For the routine neuropathological examinations, the sections were subjected to H&E or Klüver-Barrera staining. Immunohistochemistry was performed according to a standard polymer-based method using the EnVision Kit (Dako, Glostrup, Denmark). The primary antibodies used in this study were antiubiquitin (polyclonal rabbit, 1:2000; Dako, Glostrup, Denmark), anti-TDP-43 (polyclonal rabbit, 1:2500; ProteinTech, Chicago, Illinois, USA), antiphosphorylated TDP-43 (pTDP-43 ser 409/410, polyclonal rabbit, 1:2500; CosmoBio, Tokyo, Japan), anti-FUS (polyclonal rabbit, 1:500; Sigma Aldrich, St Louis, Missouri, USA), anti-α internexin (monoclonal mouse, 1:1000; Invitrogen, Carlsbad, California, USA), antiperipherin (polyclonal rabbit, 1:200; Millipore, Billerica, Massachusetts, USA), anti-CD68 (monoclonal mouse, 1:200; Dako, Glostrup, Denmark), antiphosphorylated neurofilament (pNF, monoclonal mouse, 1:600; Dako, Glostrup, Denmark) and parvalbumin (polyclonal mouse, 1:1000; Sigma Aldrich, St Louis, Missouri, USA). Diaminobenzidine (Wako, Osaka, Japan) was used as the chromogen.

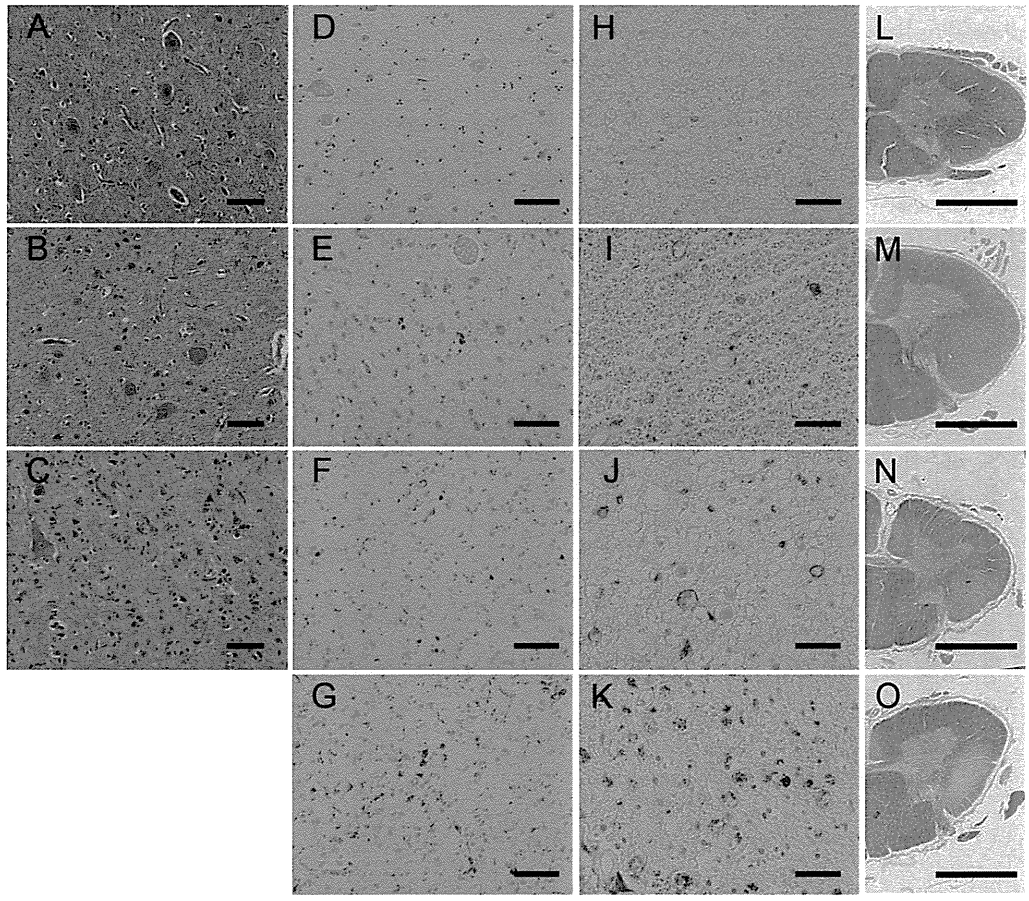

Figure 1 Measures of degeneration in the upper motor neuron system. (A–D) Loss of Betz cells in the primary motor cortex: stage (−), the Betz cells were spared in number and gliosis was absent (A); stage (+), mild neuronophagia and gliosis were noted (B) and stage (++), marked neuronophagia and glial proliferation were observed (C). (D–K) Aggregation of CD68 macrophages in the primary motor cortex (D–G) and the corticospinal tract in the lateral column of the spinal cord (H–K): stage (−), the aggregates were absent (D and H); stage (+), the aggregates were occasionally present (E and I); stage (++), the aggregates were present at a number of 1–5/ ×100 field (F and J) and stage (+++), the aggregates were diffusely observed (G and K). (L–O) Myelin pallor in the corticospinal tracts (CST) of the lateral column of the spinal cord: stage (−), myelin pallor was not detected (L); stage (+), myelin pallor was slightly notable (M); stage (++), myelin pallor was moderate (N) and stage (+++), the CST was entirely pale. (A–C) H&E staining, (D–K) anti-CD68 immunohistochemistry and (L–O) Klüver-Barrera staining. Scale bars: (A–G) 100 μm, (H–K) 50 μm and (L–O) 3 mm.

Quantitative analysis of large axonal fibres in the CST

To evaluate the degeneration of axonal fibres in the CST, we calculated the density of axonal fibres in the lateral column of the spinal cord. Specimens corresponding to the C5–6 levels were prepared for all of the patients and 13 controls. For this assay, the paraffin-embedded spinal cords were immunostained using the anti-pNF antibody and diaminobenzidine as chromogen without additional nuclear staining to visualise only axons as brown particles. The microscopic views were binarised and automatically recognised using Luzex AP software (Nireco, Tokyo, Japan) that was coupled to the microscope via a CCD video camera. This software automatically measured the particle counts and diameters on the binarised pictures.[13] Axonal counts were evaluated on five areas of 10 000 μm^2 (×40 objective) randomly chosen from the CST of the spinal lateral column in each patient and averaged. To validate duplicability between tests, we constructed two axon size histograms from 13 ipsilateral control samples (see online supplementary file). Briefly, the variability between the test and retest was sufficiently small to count the axons for each axon size. We constructed a histogram of axonal sizes in the CST (figure 2A), and the density of the large axons (axonal fibres/10 000 μm^2) was calculated (figure 2B,C) for patients with PMA and ALS and control samples.

Statistical analysis

The demographic features of patients with PMA and ALS were compared using the Mann-Whitney U test for continuous variables or the Pearson's χ^2 test or Fisher's exact test to assess bivariate correlations. The Kruskal-Wallis test was used for analyses between three groups, and the t test was used for analyses between two groups. The significance level was set at a p value of 0.05 for comparisons between two groups and 0.016 for comparisons between three groups. All of the statistical tests performed were two-sided and were conducted using the software program PASW V.18.0 (IBM SPSS).

RESULTS

Demographic features of the registered patients

The included patients consisted of 67 men and 40 women. The mean age at disease onset was 62.7 ±12.4 years, and the median duration from disease onset to death was 27 months (range 2–348 months). Seventeen patients were treated with tracheostomy positive-pressure ventilation (TPPV). Initial symptoms included upper limb weakness in 40.2%, lower limb weakness in 32.7%, bulbar symptoms in 24.3% and respiratory symptoms in 2.8% of the included patients. Fourteen (13.1%) patients were categorised into the clinical PMA group, and 93 (86.9%) patients were

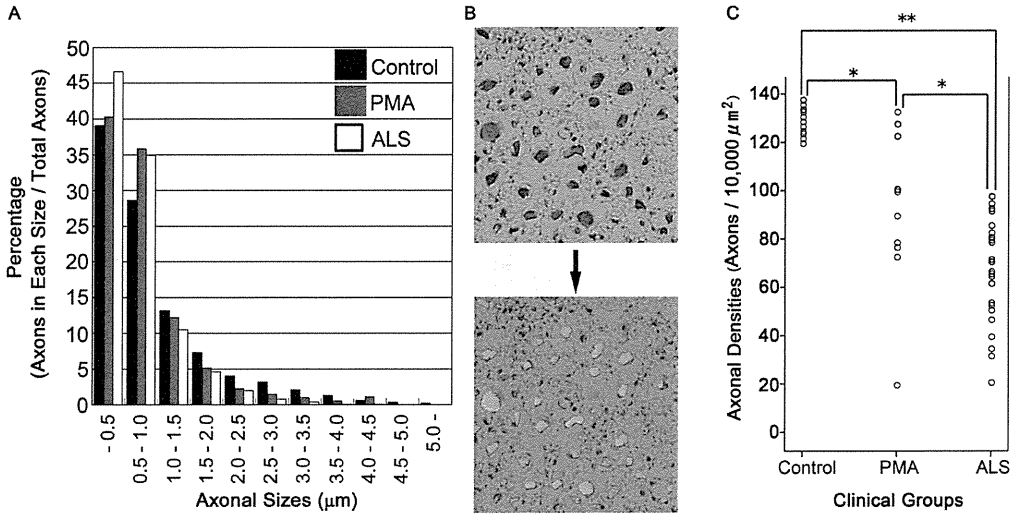

Figure 2 Quantitative analysis of the axonal fibres in the corticospinal tract. (A) Phosphorylated neurofilament (pNF)-positive fibres were automatically binarised using Luzex AP software. The density of pNF-positive axons (particles/10 000 μm^2) was automatically calculated using averaged data from five fields (×400). The histogram of axonal sizes revealed that the percentages of axons that were more than 1 μm in diameter were smaller in ALS and PMA than in controls. (B) The large axonal fibres more than 1 μm in diameter were automatically recognised, binarised and counted using the software to successfully evaluate the axonal density. (C) There were significant differences in the densities of axons that were more than 1 μm in diameter between all pairs of clinical groups: p=0.001 (*) between the clinical amyotrophic lateral sclerosis (ALS) and clinical progressive muscular atrophy (PMA) groups, p=0.001 (*) between the clinical PMA and control groups and p<0.001 (**) between the clinical ALS and control groups. All patients diagnosed with clinical ALS exhibited lower values than the controls. In contrast, the results of the clinical PMA group were widely diverse, ranging from low values to values within the normal range.

classified into the clinical ALS group. With regard to clinical diagnosis, 10 (71.4%) of 14 patients with clinical PMA and 88 (94.6%) of 93 patients with clinical ALS were correctly diagnosed as PMA or ALS by the first referred physicians. However, one patient with clinical PMA and four patients with clinical ALS were initially diagnosed as having cervical or lumbar canal stenosis based on focal weakness restricted to one upper or lower limb and canal stenosis on MRI. One of the patients with clinical PMA was initially diagnosed as having carpal tunnel syndrome based on weakness restricted to the distal area of the median nerve in the right hand. One of the patients with clinical PMA was diagnosed as having polyradiculopathy because the cauda equina was slightly enhanced on gadolinium-enhanced MRI. One of the patients with clinical PMA was initially diagnosed as having myositis based on myalgia and slight lymphatic infiltration on a muscle biopsy. One of the patients with clinical ALS was initially diagnosed as having parkinsonian syndrome because the patient showed bradykinesia due to marked rigospasticity in the limbs. The demographic features of patients with clinical PMA and ALS are presented in table 1. In summary, no significant differences in the age at onset, male-to-female ratio, clinical duration (whether including or excluding the TPPV treatment period) or initial symptoms were detected between the clinical PMA and ALS groups.

Pathological evaluations

Degeneration in the UMN system

Loss of Betz cells in the primary motor cortex

Ten (76.9%) of the 13 patients with clinical PMA exhibited a loss of Betz cells, which was severe in 3 (23.1%) of these patients (figure 3). However, in 2 (15.4%) of the 13 patients with clinical PMA, no loss of Betz cells or gliosis in the primary motor cortex was detectable. In contrast, all of the patients diagnosed with clinical ALS exhibited a loss of Betz cells, which was severe in 10 (34.5%) of the 29 patients with clinical ALS. There was no significant difference in the severity of this pathological change between the clinical groups.

Aggregation of macrophages in the primary motor cortex

The aggregation of CD68 macrophages in the primary motor cortex was detected in 10 (76.9%) of the 13 patients with clinical PMA. In contrast, all of the patients diagnosed with clinical ALS exhibited the aggregation of macrophages in the primary motor cortex. When comparing the clinical groups, this pathological change was significantly more severe in clinical ALS than clinical PMA ($p=0.048$).

CST degeneration

Myelin pallor was present in 8 (61.5%) of the 13 patients with clinical PMA. The aggregation of macrophages within the CST was detected in 11 (84.6%) of the 13 patients with clinical PMA. In the clinical ALS group, all patients exhibited myelin pallor and macrophage aggregation in the CST. When comparing the clinical groups, this pathological change was significantly more severe in clinical ALS than clinical PMA ($p=0.004$).

Degeneration in the LMN system

All of the patients diagnosed with either clinical PMA or ALS exhibited neuronal loss in the spinal anterior horns (figure 3). This neuronal loss was severe in 11 (84.6%) of the 13 patients with clinical PMA and 20 (69%) of the 29 patients with clinical ALS. All of the patients diagnosed with clinical PMA and 27 (93.1%) of the 29 patients with clinical ALS exhibited neuronal loss in the cranial nerve nuclei. This neuronal loss was severe in 6 (46.2%) of the 13 patients with clinical PMA and 11 (37.9%) of the 29 patients with clinical ALS. When comparing the clinical groups, there was no significant difference in the severity of LMN loss. Eight (61.5%) of the 13 patients with clinical PMA and 24 (82.8%) of the 29 patients with clinical ALS displayed Bunina bodies in the LMN system.

Table 1 Demographic features of clinical patients with PMA and ALS

	Clinical PMA	Clinical ALS	p Value
Number of patients	14	93	
Age at onset (years, mean±SD)	60.8±10.8	63.0±12.7	0.388*
Male/female	10/4	57/36	0.563†
Duration from onset to death (months; median, range)‡	21 (5–192)	29 (2–348)	0.764*
Initial symptoms (number of patients)			
Bulbar symptoms	3 (21.4%)	23 (24.7%)	0.738†
Upper limb weakness	5 (35.7%)	38 (40.9%)	0.738†
Lower limb weakness	5 (35.7%)	30 (32.3%)	0.738†
Respiratory symptoms	1 (7.1%)	2 (2.2%)	

*Mann-Whitney U test.
†Fisher's exact test.
‡Including the TPPV treatment period.
ALS, amyotrophic lateral sclerosis; PMA, progressive muscular atrophy; TPPV, tracheostomy positive-pressure ventilation.

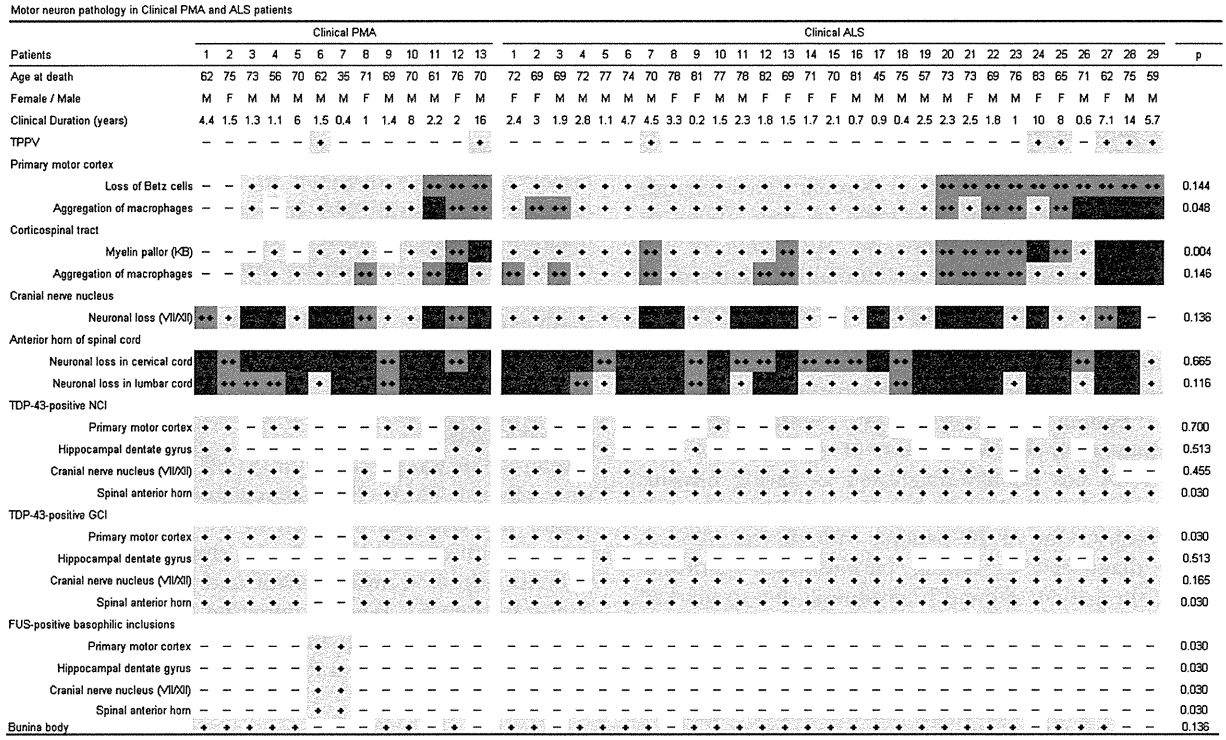

Figure 3 Summary of the neuropathological findings in the included patients. The stages of the pathological changes correspond to those in figure 1. Pathological changes between the clinical groups were compared using Pearson's χ^2 test. ALS, amyotrophic lateral sclerosis; FUS, antifused-in-sarcoma; GCI, glial cytoplasmic inclusions; KB, Klüver-Barrera staining; NCI, neuronal cytoplasmic inclusion; PMA, progressive muscular atrophy; TDP-43, 43 kDa TAR DNA-binding protein; TPPV, tracheostomy positive-pressure ventilation.

Immunohistochemical profiles

In 11 (84.6%) of the patients with clinical PMA, we detected ubiquitin and TDP-43-positive neuronal cytoplasmic inclusions (NCIs) in the LMN system (figure 3). In eight of these patients, TDP-43-positive NCIs were also detected in the primary motor cortex. All of the patients with clinical ALS displayed ubiquitin and TDP-43-positive NCIs in the LMN system. Moreover, TDP-43-positive glial cytoplasmic inclusions were observed in the spinal anterior horn and primary motor cortex in all of the TDP-43-positive patients of the clinical ALS and PMA groups. In contrast, two of the patients with clinical PMA (15.4%) exhibited basophilic inclusion bodies in the neuronal cytoplasm, which were broadly extended throughout the central nervous system. These inclusions were positive for FUS but negative for TDP-43, α-internexin and peripherin.

Quantitative analysis of large axonal fibres in the CST

The histogram of axonal sizes revealed that the percentage of axons that were greater than 1 μm in diameter was smaller in ALS (18.5%) and PMA (23.9%) than in controls (32.3%), resulting in a relative increase in the percentage of smaller axons (figure 2). Then, we measured the densities of large axons that were greater than 1 μm in diameter. The average densities were as follows: clinical ALS, 68.3±20.9 fibres/10 000 μm^2; clinical PMA, 97.2±31.5 fibres/10 000 μm^2 and controls, 129.1±6.1 fibres/10 000 μm^2 ($p=0.001$ between the clinical ALS and PMA groups; $p=0.001$ between the clinical PMA and control groups; $p<0.001$ between the clinical ALS and control groups). All patients diagnosed with clinical ALS exhibited lower values than the range of normal values that was obtained from the controls. In contrast, the results from the clinical PMA group were widely diverse. The results from 5 (38.5%) of the 13 patients with clinical PMA were within the normal range, but 8 (61.5%) of these patients exhibited lower values than the normal range. One patient with PMA who had been treated with TPPV exhibited an exceptionally low value.

Pathological overview of the patients diagnosed with clinical PMA or clinical ALS

Clinical PMA: 11 (84.6%) of the 13 patients with clinical PMA displayed UMN degeneration (either the loss of Betz cells, myelin pallor or the aggregation of macrophages in the primary cortex or CST) and LMN degeneration. Nine of these patients exhibited TDP-43-positive inclusions and the remaining 2 patients displayed FUS-positive basophilic inclusion bodies. Their large

CST axon densities were diverse, ranging from low values to values within the normal range that were obtained from the control participants. In 2 (15.4%) of the 13 patients with clinical PMA, neuropathological parameters that we defined as UMN system degeneration were all negative. Their large CST axon density was within the normal range. These two patients exhibited abundant TDP-43-positive neuronal and glial inclusions in the LMN and, occasionally, in layers II–III of the primary motor cortex and the hippocampus. The pathological findings from the representative patients are shown in figure 4.

Clinical ALS: All 29 patients displayed a combination of UMN and LMN system degeneration and exhibited TDP-43-positive inclusions.

Additionally, of the respirator-managed patients, three patients (patient 13 of clinical PMA and patients 27 and 28 of clinical ALS) showed diffusely extended neuronal loss, gliosis and TDP-43 pathology beyond the motor neuron systems, which involved all layers of the cerebral

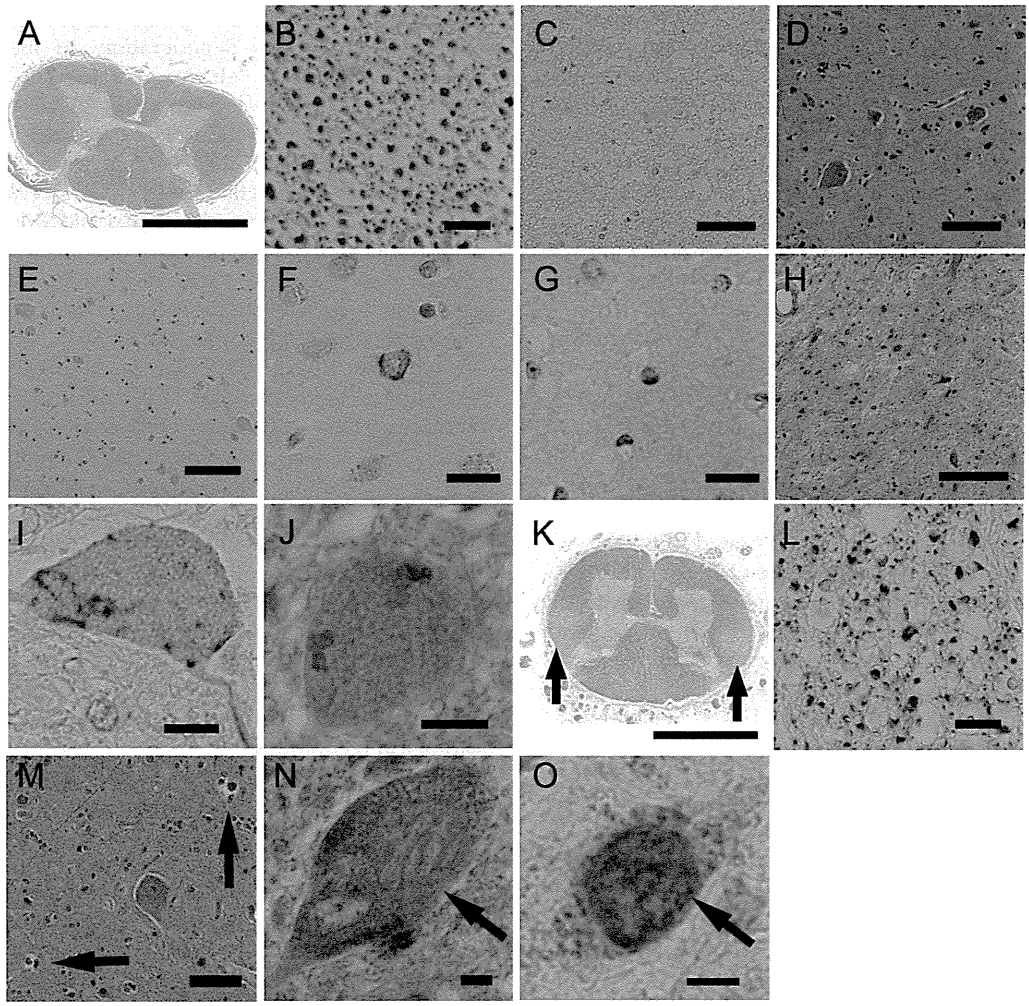

Figure 4 Neuropathological profiles of the patients in the clinical progressive muscular atrophy group. (A–J) correspond to patient 2. The corticospinal tracts (CST) did not display myelin pallor (A), loss of large axonal fibres (B), or aggregation of macrophages (C). Additionally, in the primary motor cortex, neither the loss of Betz cells (D) nor aggregation of macrophages (E) was detected. The upper layers of the primary motor cortex rarely contained phosphorylated 43 kDa TAR DNA-binding protein (pTDP-43)-positive neuronal (F) and glial (G) inclusions. The spinal anterior horn displayed severe neuronal loss (H), pTDP-43-positive skein-like inclusions (I) and Bunina bodies (J). (K–M) correspond to patient 12. The CST displayed myelin pallor (K) and the depletion of large axonal fibres (L). Neuronophagia was often found in the primary motor cortex (M, arrows). (N and O) correspond to patient 6. The spinal motor neurons contained basophilic inclusion bodies (N) that were positive for antifused-in-sarcoma (FUS) based on immunohistochemistry (O). (A and K) Klüver-Barrera staining, (B) antiphosphorylated neurofilament immunohistochemistry, (C and E) anti-CD68 immunohistochemistry, (D, H, J and M) H&E staining, (F, G and I) anti-pTDP-43 immunohistochemistry and (O) anti-FUS immunohistochemistry. Scale bars: (A and K) 3 mm, (D and E) 100 μm, (C, H and M) 50 μm, (B) 20 μm and (F, G, I, J, N and O) 10 μm.

neocortices, the striatum, thalamus, cerebellar dentate nucleus and non-motor nuclei in the brainstem, including the substantia nigra, red nucleus, periaqueductal grey matter, inferior olivary nucleus and reticular formation.

DISCUSSION

Our study demonstrated the clinicopathological profiles of patients with clinical PMA and ALS in a consecutive autopsy series. The clinical evaluations in this study revealed rapid disease progression and short survival duration in patients with clinical PMA, which are analogous courses to those that are characteristic of clinical ALS. Contrary to our results, it has been described that PMA exhibits slower progression and longer survival duration compared with ALS.[3] However, recent studies revealed that PMA follows a relentlessly progressive course and that the survival duration is not much longer than that of ALS.[2 4 9 10 14] The relatively small number of patients in our study may have contributed to the absence of significant differences in the survival durations between the clinical PMA and ALS groups.

Our pathological results indicate that, of the patients with clinical PMA, 85% exhibited degeneration in the UMN and LMN systems, which corresponds with ALS. However, the remaining 15% of patients with clinical PMA lacked any apparent degeneration in the UMN system. A previous study reported that approximately 50% of all patients with PMA exhibit macrophages in the CST.[5] Another report demonstrated the degeneration of the pyramidal tract and loss of Betz cells in 65% and 60%, respectively, of the patients diagnosed with the PMA phenotype.[6] Our results revealed that patients with PMA more frequently had degeneration in the UMN system than those reported in previous studies; however, in a few patients with PMA, UMN degeneration remained undetectable at death. Our pathological results revealed differential UMN involvement between patients with PMA and indicated that PMA and ALS are continuous pathological entities. Regarding immunohistochemical aspects, several studies have revealed that TDP-43 pathology is commonly observed in the cerebral cortices or the subcortical grey matter of patients with PMA.[7 8] In our results, TDP-43-positive neuronal or glial inclusions in the motor cortices or hippocampus were common in the clinical ALS and PMA groups and were found even in patients apparently lacking UMN degenerative changes. A recent report described the propagation of TDP-43 pathology in ALS, which starts from the UMN and LMN systems and spreads to the anteromedial temporal lobes through the motor neuron system.[15] Based on this theory of TDP-43 propagation, TDP-43 pathology beyond the LMN system in patients with PMA may support the pathological continuity between these two clinical phenotypes.

The standard diagnostic criteria for ALS are the revised El Escorial criteria, which require a combination of UMN and LMN symptoms/signs for the diagnosis of ALS.[12] However, it is often difficult to clinically determine whether the UMN is involved,[16] which sometimes results in diagnostic difficulty. In our patient series, only 71.4% of the patients with clinical PMA were correctly diagnosed by the first referred physicians, although 94.6% of the patients with clinical ALS were diagnosed correctly. Recently, several studies have demonstrated the utility of radiological procedures, including transcranial magnetic stimulation, ^{1}H MR spectroscopy and diffusion tensor imaging in the detection of UMN system deterioration in a subset of patients with PMA.[14 17–20] Based on our results, a large subset of patients with PMA may have some degree of UMN degeneration. In such patients, these radiological or electrophysiological procedures would be expected to increase the sensitivity of detection of UMN degeneration. However, our results also indicate that some of the patients with PMA exhibit sparse morphological changes in the UMN system, even at death. It may be difficult to detect UMN degeneration using these procedures in such patients. To diagnose clinical patients with PMA displaying sparse UMN degeneration as ALS in the early phase of the disease course may be a future subject of focus.

A limitation of our study was the inability to evaluate the entire motor cortex and CST, and it is controversial whether patients with apparently intact UMN systems actually lack or have extremely mild UMN involvement. Another methodological limitation is that we evaluated axonal sizes and densities using neutral formalin-fixed, paraffin-embedded specimens. The tissues may be somewhat distorted when compared with conventional nerve fixation using glutaraldehyde followed by Epon embedding. Our methods were considered to be appropriate to assess the proportional changes in the sizes of pyramidal axons, but the absolute values of axonal diameters can vary from those that have been obtained using other histological techniques.[13]

In summary, 84.6% of patients with clinical PMA displayed UMN and LMN degeneration, which is consistent with the pathological profiles of ALS. In 15.4% of the patients with clinical PMA, degeneration in the UMN system was undetectable. The large axon density in the CST varied from low values to a normal range. In contrast, all of the clinical patients with ALS displayed a combination of UMN and LMN system degeneration and significantly reduced large axon density in the CST.

Acknowledgements The authors specially thank Dr M Hasegawa, Department of Neuropathology and Cell Biology, Tokyo Metropolitan Institute of Medical Science, for performing the genetic analysis of the fused-in-sarcoma (FUS) genes.

Contributors YR and NA contributed to the conception and design of the study. All of the authors participated in the acquisition, analysis and interpretation of the data. MY and GS drafted the manuscript. MI and HW assisted in writing and editing the manuscript.

Funding This work was supported by Grants-in-Aid from the Research Committee of CNS Degenerative Diseases of the Ministry of Health, Labor, and Welfare of Japan.

Competing interests None.

Ethics approval This study was approved by the ethics committees of Nagoya University and Aichi Medical University.

Provenance and peer review Not commissioned; externally peer reviewed.

Data sharing statement No additional data are available.

REFERENCES

1. Neumann M, Sampathu DM, Kwong LK, *et al.* Ubiquitinated TDP-43 in frontotemporal lobar degeneration and amyotrophic lateral sclerosis. *Science* 2006;314:130–3.
2. de Carvalho M, Scotto M, Swash M, *et al.* Clinical patterns in progressive muscular atrophy (PMA): a prospective study. *Amyotroph Lateral Scler* 2007;8:296–9.
3. Norris FH. Adult progressive muscular atrophy and hereditary spinal muscular atrophies. In: Vinken PJ, Bruyn GW, Klawans HL, De Jong JMBV, eds. *Handbook of clinical neurology: diseases of the motor system.* Vol 59. Amsterdam: North-Holland Publishing Company, 1991:13–34.
4. Visser J, van den Berg-Vos RM, Franssen H, *et al.* Disease course and prognostic factors of progressive muscular atrophy. *Arch Neurol* 2007;64:522–8.
5. Ince PG, Evans J, Knopp M, *et al.* Corticospinal tract degeneration in the progressive muscular atrophy variant of ALS. *Neurology* 2003;60:1252–8.
6. Brownell B, Oppenheimer DR, Hughes JT. The central nervous system in motor neurone disease. *J Neurol Neurosurg Psychiatry* 1970;33:338–57.
7. Geser F, Stein B, Partain M, *et al.* Motor neuron disease clinically limited to the lower motor neuron is a diffuse TDP-43 proteinopathy. *Acta Neuropathol* 2011;121:509–17.
8. Nishihira Y, Tan CF, Hoshi Y, *et al.* Sporadic amyotrophic lateral sclerosis of long duration is associated with relatively mild TDP-43 pathology. *Acta Neuropathol* 2009;117:45–53.
9. Kim WK, Liu X, Sandner J, *et al.* Study of 962 patients indicates progressive muscular atrophy is a form of ALS. *Neurology* 2009;73:1686–92.
10. Van den Berg-Vos RM, Visser M, Kalmijn S, *et al.* A long-term prospective study of the natural course of sporadic adult-onset lower motor neuron syndromes. *Arch Neurol* 2009;66:751–7.
11. Koike H, Hirayama M, Yamamoto M, *et al.* Age associated axonal features in HNPP with 17p11.2 deletion in Japan. *J Neurol Neurosurg Psychiatry* 2005;76:1109–14.
12. Brooks BR, Miller RG, Swash M, *et al.* El Escorial revisited: revised criteria for the diagnosis of amyotrophic lateral sclerosis. *Amyotroph Lateral Scler Other Motor Neuron Disord* 2000;1:293–9.
13. Sobue G, Hashizume Y, Mitsuma T, *et al.* Size-dependent myelinated fiber loss in the corticospinal tract in Shy-Drager syndrome and amyotrophic lateral sclerosis. *Neurology* 1987;37:529–32.
14. Mitsumoto H, Ulug AM, Pullman SL, *et al.* Quantitative objective markers for upper and lower motor neuron dysfunction in ALS. *Neurology* 2007;68:1402–10.
15. Brettschneider J, Del Tredici K, Toledo JB, *et al.* Stages of pTDP-43 pathology in amyotrophic lateral sclerosis. *Ann Neurol* 2013;74:20–38.
16. Swash M. Why are upper motor neuron signs difficult to elicit in amyotrophic lateral sclerosis? *J Neurol Neurosurg Psychiatry* 2012;83:659–62.
17. Sach M, Winkler G, Glauche V, *et al.* Diffusion tensor MRI of early upper motor neuron involvement in amyotrophic lateral sclerosis. *Brain* 2004;127:340–50.
18. Vucic S, Ziemann U, Eisen A, *et al.* Transcranial magnetic stimulation and amyotrophic lateral sclerosis: pathophysiological insights. *J Neurol Neurosurg Psychiatry* 2013;84:1161–70.
19. Graham JM, Papadakis N, Evans J, *et al.* Diffusion tensor imaging for the assessment of upper motor neuron integrity in ALS. *Neurology* 2004;63:2111–19.
20. Prudlo J, Bißbort C, Glass A, *et al.* White matter pathology in ALS and lower motor neuron ALS variants: a diffusion tensor imaging study using tract-based spatial statistics. *J Neurol* 2012;259:1848–59.

Disease causing mutants of TDP-43 nucleic acid binding domains are resistant to aggregation and have increased stability and half-life

James A. Austin[a,1], Gareth S. A. Wright[a,1], Seiji Watanabe[b], J. Günter Grossmann[a], Svetlana V. Antonyuk[a], Koji Yamanaka[b], and S. Samar Hasnain[a,2]

[a]Molecular Biophysics Group, Institute of Integrative Biology, Faculty of Health and Life Sciences, University of Liverpool, Liverpool L69 7ZB, United Kingdom; and [b]Department of Neuroscience and Pathobiology, Research Institute of Environmental Medicine, Nagoya University, Nagoya, Aichi 464-8601, Japan

Edited by Gregory A. Petsko, Weill Cornell Medical College, New York, NY, and approved February 6, 2014 (received for review September 14, 2013)

Over the last two decades many secrets of the age-related human neural proteinopathies have been revealed. A common feature of these diseases is abnormal, and possibly pathogenic, aggregation of specific proteins in the effected tissue often resulting from inherent or decreased structural stability. An archetype example of this is superoxide dismutase-1, the first genetic factor to be linked with amyotrophic lateral sclerosis (ALS). Mutant or posttranslationally modified TAR DNA binding protein-32 (TDP-43) is also strongly associated with ALS and an increasingly large number of other neurodegenerative diseases, including frontotemporal lobar degeneration (FTLD). Cytoplasmic mislocalization and elevated half-life is a characteristic of mutant TDP-43. Furthermore, patient age at the onset of disease symptoms shows a good inverse correlation with mutant TDP-43 half-life. Here we show that ALS and FTLD-associated TDP-43 mutations in the central nucleic acid binding domains lead to elevated half-life and this is commensurate with increased thermal stability and inhibition of aggregation. It is achieved without impact on secondary, tertiary, or quaternary structure. We propose that tighter structural cohesion contributes to reduced protein turnover, increasingly abnormal proteostasis and, ultimately, faster onset of disease symptoms. These results contrast our perception of neurodegenerative diseases as misfolded proteinopathies and delineate a novel path from the molecular characteristics of mutant TDP-43 to aberrant cellular effects and patient phenotype.

motor neuron disease | oligemisation | SAXS | protein degradation

The fatal course of age-related neurological disorders is often presaged and accompanied by protein destabilization leading to abnormal aggregation (1). A classic example is the protein superoxide dismutase-1 (SOD1); loss of structural stability (2) and increased aggregation propensity (3) are determinants of the disease course for people with amyotrophic lateral sclerosis (ALS) with mutations in the SOD1 gene (4). TAR DNA binding protein 43 (TDP-43) is associated with ALS (5, 6) but is also implicated in an increasingly large number of other neurological diseases, including frontotemporal lobar degeneration with ubiquitin-associated inclusions (FTLD-U) (7), Alzheimer's disease (8), and Guam-Parkinsonism dementia (9). This justifies TDP-43's position as a high value target but its involvement in familial and sporadic forms of disease doubly underscores this.

TDP-43 was first shown to bind and inhibit transcription of TAR DNA (10) but has since been linked with several other nucleic-acid–binding functions, such as transport (11), stress granule formation (12), and translation (13). Most importantly, TDP-43 is known to bind, stabilize, and regulate the splicing of a huge number of mRNAs, including its own (14–17). It is understandable therefore that targeted TDP-43 knockout or overexpression leads to motor neuron disease-like symptoms in mice (18, 19). These facts indicate that strict control of available TDP-43 is critical; however, ALS mutant TDP-43 proteins have been shown to have increased half-life in cell models (20, 21). Additionally, there is a good relationship between increased half-life and rapid disease onset, which links in vivo TDP-43 behavior with observable patient phenotypes (20).

Like FUS, TDP-43's function is reliant on its ability to bind DNA/RNA targets (17, 22, 23). This is accomplished by two centrally located RNA recognition motif (RRM) domains (24), which are also important for normal localization of TDP-43 to nuclear Gems (25). Furthermore, whole RRM domains, or sections thereof, are important modifiers of TDP-43 toxicity and are involved in the formation of aggregated cytoplasmic C-terminal fragments (26–29). Two disease-associated mutations are found within TDP-43's RRM domains: D169G and K263E. The D169G ALS mutant (6) has previously been used to assess mutant stress granule formation (30). This process requires functional nucleic acid binding and is unaffected by the D169G mutation (30, 31). It is situated in loop 5 of RRM1 between α-helix 2 and β-strand 4. The FTLD-U–associated K263E mutant (32) is found immediately after RRM2 and is part of the nucleic acid binding site (33).

In this study, we show that disease-related RRM domain mutants exhibit a significant increase in thermal stability in vitro, with D169G being the most stable. This correlates with increased resistance to in vitro aggregation and protraction of their half-life in a TDP-43 disease cell model. We also show that these mutants do not cause oligomerization, significant conformational changes, aberrant domain interactions, or unfolding, as is the case for the majority

Significance

Adult onset neurodegenerative diseases are viewed as protein destabilization, misfolding, and aggregation diseases. TAR DNA binding protein-43 (TDP-43) protein is strongly associated with many neurological disorders, particularly amyotrophic lateral sclerosis and frontotemporal lobar degeneration. All of the disease-associated TDP-43 mutants tested have been shown to increase TDP-43 half-life and this correlates inversely with the age at which the sufferer first becomes aware of symptoms. Here we show that disease mutations in two TDP-43 nucleic acid binding domains also increase the protein's half-life and this is commensurate with increased structural stability and resistance to aggregation. Our results are an unusual contrast to other neurodegenerative diseases and provide a potential link between the molecular characteristics of mutant TDP-43 and the symptoms of these debilitating diseases.

Author contributions: J.A.A., G.S.A.W., S.W., S.V.A., K.Y., and S.S.H. designed research; J.A.A., G.S.A.W., S.W., and J.G.G. performed research; J.A.A., G.S.A.W., S.W., S.V.A., K.Y., and S.S.H. analyzed data; and J.A.A., G.S.A.W., K.Y., and S.S.H. wrote the paper.

The authors declare no conflict of interest.

This article is a PNAS Direct Submission.

Freely available online through the PNAS open access option.

[1]J.A.A. and G.S.A.W. contributed equally to this work.

[2]To whom correspondence should be addressed. E-mail: S.S.Hasnain@liverpool.ac.uk.

This article contains supporting information online at www.pnas.org/lookup/suppl/doi:10.1073/pnas.1317317111/-/DCSupplemental.

NEUROSCIENCE

of neurodegenerative-disease–causing proteins (34). Our results add countenance to the notion that disease-related TDP-43 mutations increase the protein's half-life regardless of location and pose the question, "Could increased TDP-43 half-life result from tighter structural cohesion and the resistance to degradation that it would confer?"

Results

TDP-43 RRM Mutant Proteins Have Abnormally Elevated Half-Life. In a previous study, we revealed that increased stability of TDP-43 causes toxicity through abnormal proteostasis and RNA dysregulation (20). Several TDP-43 mutants have now been found to confer increased half-life in cell models (20, 21). However, to date, only mutants in the C-terminal glycine-rich tail have been analyzed. To examine whether RRM disease mutants are likely to affect TDP-43 stability in vivo, a pulse-chase labeling of D169G and K263E full-length human TDP-43 mutants was performed using the methionine analog L-azidohomoalanine in a cell culture model.The half-lives of these RRM disease mutants [$T_{1/2}$ = 43.7 ± 7.0 h (D169G), 29.6 ± 6.2 h (K263E)] were distinctly longer than that of wild type ($T_{1/2}$ = 14.7 ± 1.5 h) (Fig. 1). These results indicate that increased half-life is a common property of disease-causing TDP-43 mutations regardless of the location in the primary structure and suggest a common mechanism for their toxicity.

Disease-Causing TDP-43 RRM Mutants Resist Thermal Unfolding. In vitro study of TDP-43 RRM domains is now well established (24, 26, 35) and presents the opportunity to investigate potential reasons for the observed increase in cellular half-life at the macromolecular level using a variety of biophysical techniques. Mouse TDP-43 shares 93% sequence identity with human TDP-43 between residues 101 and 265 (TDP-43S) (Fig. S1). The majority of differences occur within the RRM2 domain (residues 192–265) and both Asp169 and Lys263 are conserved between species. Due to the high degree of sequence identity, structural changes are likely to strongly correlate between homologs and the mouse protein can be used as a representative model system.

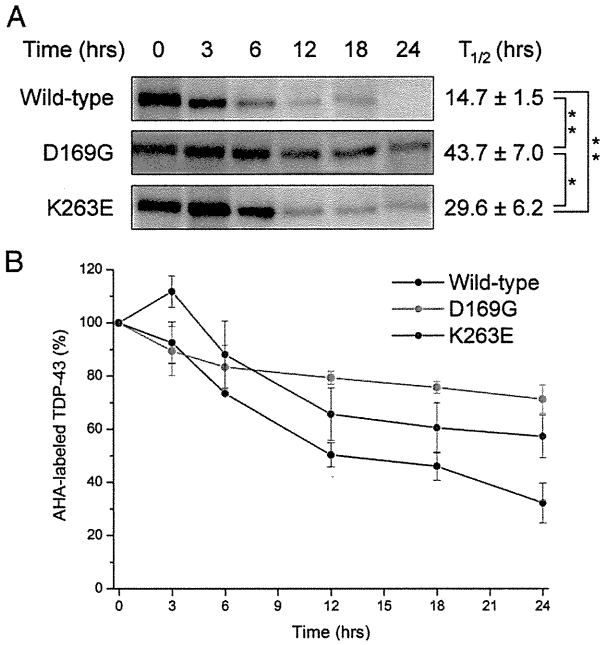

Fig. 1. Increased half-lives of ALS/FTLD-linked RRM mutant full-length TDP-43 proteins in cultured cells. (*A*) Transfected Neuro2a cells were metabolically labeled with L-azidohomoalanine (AHA). AHA-labeled TDP-43 was immunoprecipitated and visualized as described in *Materials and Methods*. (*B*) The averages of three independent experiments are plotted. Error bars represent SE of mean (SEM). Half-lives of the proteins were calculated by curve fitting (*A*, *Right*) and expressed as means ± SEM from three independent experiments. The data were analyzed by one-way ANOVA followed by Tukey–Kramer post hoc tests. *$P < 0.05$, **$P < 0.01$.

Susceptibility to thermal and chemical unfolding is a common characteristic of proteins involved in neurodegeneration (36–39). This is exemplified by ALS SOD1 mutations, which are detrimental to protein stability, cause unfolding resulting in the exposure of hydrophobic regions, and increase the protein's aggregation potential (37, 40). The unfolding temperature (T_m) of mTDP-43S has previously been determined by circular dichroism (CD) as 49.7 °C (24). To compare the thermal stability of wild-type mTDP-43S with the two point mutations described, differential scanning fluorimetry (DSF) and aromatic fluorescence were used to monitor their unfolding (41, 42).

The changes in Sypro-orange fluorescence resulting from quenching and dequenching as the protein unfolds were measured for wild type, K263E, and D169G TDP-43S (Fig. 2*A*). Wild-type TDP-43S shows a melting transition (T_m) at 49.15 ± 0.16 °C, which is similar to the value obtained by CD spectroscopy (24). The melting transition was elevated by the K263E mutation to 50.2 ± 0.24 °C. However, an increase of 3.5 °C to a T_m of 52.64 ± 0.11 °C was observed for the D169G variant. In each case, a decline in the fluorescent signal at high temperature can be explained by aggregation of the protein (41). The increase in structural stability conferred by D169G and K263E mutations was confirmed using aromatic fluorescence over a temperature range of 37–65 °C (Fig. 2*B*). These data show two features, an increase in aromatic quenching up to 42 °C and subsequent dequenching to above the initial value. A Boltzmann fit was applied to the normalized unfolding values (Fig. 2*C*) giving melting transitions of 52.5 ± 0.9, 55.8 ± 0.8, and 58.7 ± 2.8 °C for wild type, K263E, and D169G, respectively.

A central aspect of TDP-43 functionality is its ability to bind nucleic acid and it is known to have a strong preference for UG-rich mRNA (17). Fig. 2*A*, *Top* shows how the addition of increasing length TG repeat DNA affects the unfolding transition of wild-type TDP-43. The initial melting temperature of the apo protein rises to 50.65 ± 1.17, 57.74 ± 1.02, and 62.35 ± 0.32 °C when complexed with stoichiometric amounts of TG4, TG8, and TG16 DNA, respectively. Complex formation with DNA also consistently increased the stability of the D169G mutant with melting temperatures of 54.18 ± 1.15, 59.65 ± 0.42, and 65.35 ± 0.39 °C (Fig. 2*A*, *Middle*). The K263E–TG4 complex is found to be 2.4 °C more stable than the wild-type complex; however, the stability of this mutant does not increase in the same manner observed for wild type and D169G, with the addition of longer repeat DNA; the K263E–TG8 and –TG16 complexes have melting temperatures of 57.78 ± 0.83 and 61.60 ± 0.23 °C, respectively (Fig. 2*A*, *Bottom*). This indicates that the K263E mutant may have reduced affinity for long chain nucleic acids. In support of this, Lys263 has recently been shown to intercalate between bound RNA bases, and mutation to alanine reduces binding affinity (33).

RRM Mutant TDP-43S Is Resistant to Heat-Induced Aggregation. Small angle X-ray solution scattering (SAXS) is a powerful technique to probe the overall conformation and aggregation state of macromolecules in solution (43). Here, SAXS was used to assess differences in aggregation potential between mutant and wild-type TDP-43 at two temperatures: 20 °C and 40 °C. Guinier approximations yielded radii of gyration (Rg) values of 25.8 ± 5.3, 23.3 ± 5.2, and 25.0 ± 3.9 Å, respectively, for wild type, K263E, and D169G at 20 °C. At 40 °C, these were found to be 40.1 ± 1.9, 25.7 ± 5.5, and 24.5 ± 5.1 Å (Fig. 3). The Rg of the wild-type TDP-43S shows a large increase at 40 °C, suggestive of extensive aggregation, as opposed to essentially unchanged values for the

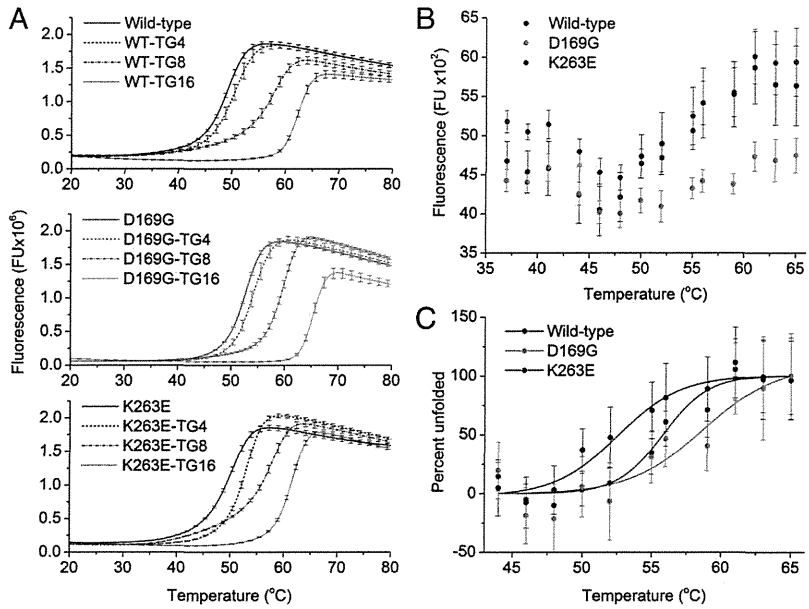

Fig. 2. Resistance of TDP-43 RRM mutants to heat-induced unfolding. (*A*) TDP-43S unfolding monitored by differential scanning fluorimetry. Sypro-orange fluorescence was monitored as a function of temperature in the absence and presence of TG repeat single-strand DNA for each TDP-43S variant. Error bars indicate SE calculated from eight replicates. Melting transitions for the apo protein, TG4-, TG8-, and TG16-bound complexes were calculated to be 49.15 ± 0.16, 50.65 ± 1.17, 57.74 ± 1.02, and 62.35 ± 0.32 °C for wild type; 52.64 ± 0.11, 54.18 ± 1.15, 59.65 ± 0.42, and 65.35 °C for D169G; and 50.20 ± 0.24, 53.05 ± 0.3, 57.78 ± 0.83, and 61.6 ± 0.23 for K263E °C. (*B*) Thermal unfolding of TDP-43S variants monitored by aromatic fluorescence. Two features are prominent: aromatic quenching beginning at 42 °C followed by dequenching at 48 °C. (*C*) Normalized unfolding curves. The melting temperature (T_m) of wild type, K263E, and D169G is 52.5 ± 0.9, 55.8 ± 0.8, and 58.7 ± 2.8 °C, respectively.

mutants. Therefore, both mutants appear resistant to heat-mediated aggregation. An explanation can be found in our observation that wild-type TDP-43S unfolding occurs at a lower temperature and this leads to an increased aggregation propensity.

RRM Mutations Do Not Engender Aberrant Oligomerization or Large Structural Changes. SAXS has previously been used to detect significant structural changes that occur due to disease-causing mutations in SOD1 (2, 44). Using SAXS, size exclusion chromatography (SEC), and CD, here we demonstrate that the secondary, tertiary, and quaternary structure of wild-type mTDP-43S is conserved when mutated. Mutant and wild-type TDP-43S elute concomitantly from a size exclusion chromatography column as single symmetrical peaks between myoglobin (17 kDa) and the SOD1 dimer (32 kDa) (Fig. 4*A* and Figs. S2 and S3). Binding of TG4 or TG8 repeat DNA causes an increase in hydrodynamic radius but the oligomeric state is maintained for each mutant (Fig. 4*A*). Fig. 4*B* shows the 1D scattering curves of TDP-43S variants obtained by SEC-SAXS. Radii of gyration of 21.9, 22.4, and 22.6 ± 0.5 Å for wild type, K263E, and D169G, respectively are slightly lower than those collected by static SAXS measurements and reflect the ability of SEC-coupled SAXS to isolate scattering from the species of interest (45). Molecular weight estimations from experimental SAXS data (46) predict a protein mass of 22 kDa, close to its theoretical monomer mass of 19 kDa. These data are consistent with TDP-43S being monomeric and that TDP-43 RRM mutations do not promote aberrant oligomerization. This correlates well with observations of human TDP-43 RRM truncation proteins (26) and as such no symmetry constraints were applied during subsequent 3D modeling.

The distance distribution function (p(r)) for mTDP-43S gives insight into the maximum dimension (D_{max}) and the average electron distribution for both mutant and wild type (Fig. S4). The D_{max} for wild-type mTDP-43S was calculated at 85.5 ± 5 Å which, when modeled, revealed two density-rich regions characteristic of tandem domains (Fig. 4*D*). Scattering curves and p(r) functions for each mutant are identical to those of the wild-type form, indicating conservation of protein structure. Similarly, when complexed with TG8 DNA the scattering curves for each TDP-43S variant can be superimposed on each other and closely resemble the computed scattering by human TDP43S with RNA bound (Fig. 4*C* and Fig. S5) (33). The radii of gyration for these protein–DNA complexes was found to be ~21 Å and D_{max} 70 Å (Fig. S6). These size parameters indicate that the DNA bound form is more compact than the apo protein and confirms observations by NMR that nucleic acid binding promotes interaction between the two RRM domains (33). To assess the arrangement of the individual RRM domains in solution in the absence of nucleic acid, a pseudoatomic model was built by rigid body refinement constrained by our experimental SAXS data

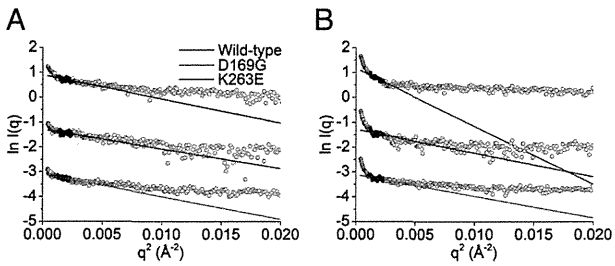

Fig. 3. Inhibition of TDP-43S aggregation by RRM ALS/FTLD-U mutations. (*A*) Guinier plots of TDP-43S variants at 20 °C. Radii of gyration are 25.8 ± 5.3, 23.3 ± 5.2, and 25.0 ± 3.9 Å for wild type, K263E, and D169G, respectively. (*B*) Guinier plots of TDP-43S variants at 40 °C. The Rg of each variant increases to 40.1 ± 1.9, 25.7 ± 5.5, and 24.5 ± 5 Å. respectively.

NEUROSCIENCE

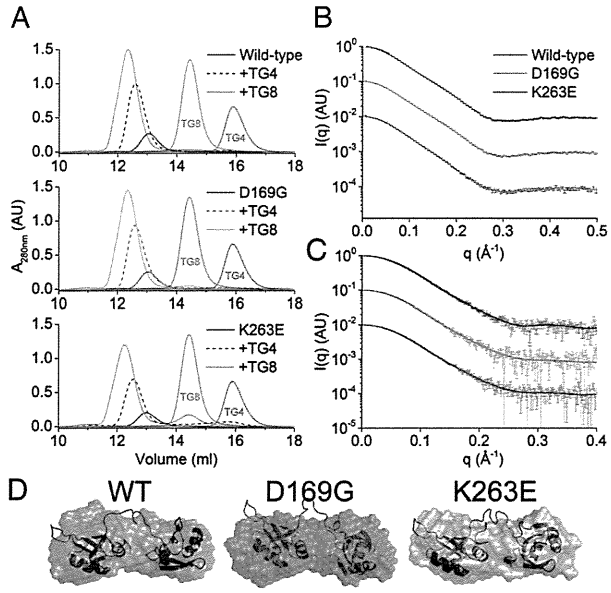

Fig. 4. Determination of the oligomeric state and conformation of TDP-43S variants. (*A*) Size exclusion chromatograms of TDP-43 variants in the absence or presence of TG4 or TG8 DNA. A total of 12.5 nmol of TDP-43 was loaded with or without a 1:1 molar ratio of DNA. TG4 and TG8 repeat single-strand DNA elute from the Superdex 75 10/300 column at 16 and 14.5 mL, respectively (purple and green). Standard elution is as follows: BSA 10.3 mL, SOD1 12.1 mL, and myoglobin 13.5. (*B*) SAXS curves for wild-type and mutant TDP-43S giving radii of gyration 21.9, 22.4, and 22.6 ± 0.5 Å for wild type, K263E, and D169G, respectively. (*C*) TG8-bound TDP-43S giving radii of gyration 21.3, 21.0, and 21.3 ± 0.5 Å, respectively. (*D*) Bead and rigid body models for TDP-43S variants. Models were generated with GASBOR ($1.7 < \chi^2 < 8.2$) and BUNCH ($\chi^2 = 2.9$, 5.1 and 2.3 respectively) without imposition of symmetry constraints.

(Fig. 4*D*). TDP-43 RRM domains have previously been suggested to behave as separate entities (35) and this appears to be the case for both disease mutants and wild type.

To substantiate our conclusion that the integrity and conformation of TDP-43S is maintained by mutation, the optical activity of each protein was determined at 20 °C by synchrotron radiation CD spectroscopy. Fig. 5 shows the CD spectra, which have good agreement with previously published work (24) but due to the higher intensity of synchrotron light, we are able to reliably show features in the vacuum UV range. The absorption spectra show little difference and the proportions of structural motifs for each variant indicates their secondary structure to be identical within the limits of error. Our results suggest these point mutations do not cause large structural changes and that differences in thermal stability, inhibition of aggregation, and protein turnover are more likely to occur through subtle structural changes at the atomic level.

Discussion

In recent years TDP-43 has been discovered to be the cause of several common neurodegenerative diseases (47). The number of conditions that are linked to TDP-43 malfunction increases on a seemingly monthly basis and this underscores the notion that neurological diseases often cannot be classified into discrete subcategories but manifest with a spectrum of symptoms. Whereas this seems daunting to those involved in biomedical research it may actually be a boon. Rather than addressing every disease state individually we may be able to effect changes in a single protein that are therapeutic across a whole disease spectrum. As such, finding unifying pathological themes is a worthy goal.

The results presented here indicate that ALS and FTLD-U mutations within the TDP-43 RRM domains do not affect the monomeric state or induce deleterious RRM interdomain interactions, global conformational changes, or unfolding. This is true in the apo or nucleic-acid–bound state. They do however confer resistance to temperature-induced unfolding, aggregation, and degradation. A correlation between increased in vitro thermal stability and increased cellular half-life has been observed for a wide range of proteins (48, 49) including point mutations in nucleic acid binding proteins (50). This indicates there may be a mechanistic link between the observed characteristics of TDP-43 mutants. The ALS-associated mutant, D169G, displayed the largest resistance to thermal unfolding, aggregation, and a half-life almost three times that of the control. In the presence of DNA, this mutant was consistently more stable than the wild type, indicating that its affinity for nucleic acid is unchanged. It is worth noting given its longer half-life, that this mutation caused a faster disease progression compared with other ALS mutations in the same study (6). Asp169 is located on loop 6 of the RRM1 structure, separating α-helix 2 and β-strand 4 with potential hydrogen bond interactions with the side chains of Lys114 and Thr115. The substitution of acidic aspartate for nonpolar glycine at this position would abrogate these bonds but may facilitate a tighter association of loop 6 with the hydrophobic inner core orchestrating the increase in stability. The K263E mutant was also shown to increase thermal stability by up to 3 °C in the apo state, which was unexpected due to its location outside of the RRM2 structure. This residue is part of the nucleic-acid–binding region (33) and the polarity change from negative to positive may aid in forming electrostatic interactions to local positive residues within the nucleic-acid–binding interface conferring a small change in stability. Like wild-type and D169G TDP-43S, K263E stability rises as the length of bound DNA increases. However, after 16 base pairs (TG8), the stability of the protein complex is less than that of the wild-type protein, indicating a reduced affinity for long nucleic acids.

Pathological posttranslational modifications such as phosphorylation (51) and cleavage (52) are currently the best explanation for those TDP-43 proteinopathy cases that occur without

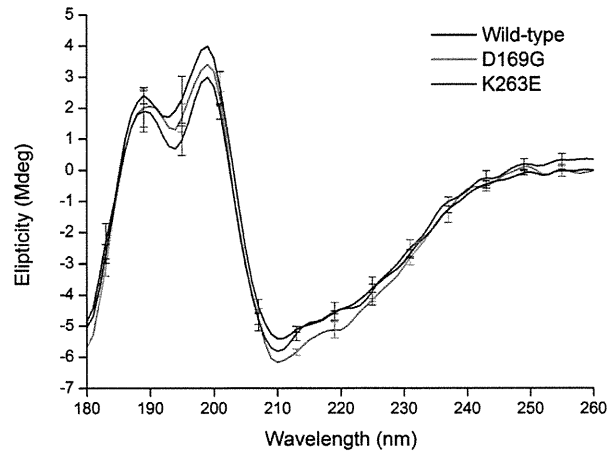

Fig. 5. Circular dichroism spectra of wild-type, D169G, and K263E TDP-43S variants. Superimposition of the spectra indicates conserved secondary. This is confirmed by secondary structure content prediction using the DichroWeb server, which gives 6, 6, and 5% α-helix for wild type, K263E, and D169G, respectively. All three variants were found to have 40% β-sheet. Normalized rmsd is 0.092, 0.101, and 0.089, respectively.

primary sequence mutation. These modifications predominate in the cytoplasmic inclusions found in affected cells and as a result were thought to initiate the aggregation cascade and lead to cell death (53). However, TDP-43 aggregation and nuclear depletion are not necessary for toxicity (54, 55). Phosphorylation of C-terminal fragments was found to increase their half-life from 14.2 to 22.1 h, indicating there may be a common toxic pathway for seemingly sporadic and familial disease forms (56). Interestingly the toxicity of some C-terminal mutations was shown to depend upon the presence and function of the RRM1 domain. When RRM1 was removed, an increase in *Drosophila* survival was observed (29), possibly by allowing more efficient degradation.

Protein unfolding and accumulation is now a well-characterized feature of neurodegenerative disease (57). A typical example of this is SOD1-related ALS where toxic SOD1 protein aggregation is thought to arise through mutation-induced protein instability and the exposure of hydrophobic regions buried within the structure (37, 40). The hypothesis that arises from the work presented here offers an interesting comparison; mutant TDP-43 becomes more stable, resists degradation, and its increased longevity changes the delicate balance of protein expression regulation, eventually leading to faster disease presentation. What remains to be established is whether other mutations throughout the TDP-43 primary structure elicit the same effect and if the posttranslational modifications thought to cause the largest subset of TDP-43 proteinopathies follow a similar route to toxicity. The finding that TDP-43 mutations promote complex formation with FUS (21) means we should not limit our search to stabilization of individual domains or even the TDP-43 monomer. The structural integrity of the dimer and complexes with RNA or other ribonucleoproteins, especially given the clustering of disease mutations in the C terminus, may all play important roles.

Materials and Methods

Pulse-Chase Assay by Chemical Labeling of Newly Synthesized Proteins. Full-length human TDP-43 cDNA was cloned into a pF5K CMV-neo Flexi mammalian expression vector as described previously (20) and RRM mutations were incorporated by site-directed mutagenesis. Neuro2a cells were grown in Dulbecco's modified Eagle's medium (DMEM) supplemented with 10% (vol/vol) FBS, 100 units/mL penicillin, 100 μg/mL streptomycin, and 2 mM glutamine in a humidified atmosphere containing 5% (vol/vol) CO_2 at 37 °C. Pulse-chase assay was performed as described previously (20) with slight modifications. Briefly, Neuro2a cells seeded at 2.0×10^5 /mL in poly-D-lysine–coated six-well plates were transiently transfected with pF5K-TDP-43 expression vectors by Lipofectamine 2000. After 6 h of incubation, the culture medium was replaced with methionine- and leucine-free DMEM supplemented with 2% (vol/vol) dialyzed FBS, 0.8 mM L-leucine, 2 mM glutamine, and 2 mM N^6,2′-O-dibutyrylguanosine 3′,5′-cyclic monophosphate sodium salt. The cells were further incubated overnight to eliminate intracellular methionine. Newly synthesized TDP-43 proteins were labeled with AHA and reacted with PEG4 carboxamide-propargyl biotin in the presence of Tris-(2-Carboxyethyl)phosphine, Tris[(1-benzyl-1H-1, 2, 3-triazol-4-yl)methyl]amine, and $CuSO_4$ at room temperature for 1 h. AHA-labeled TDP-43 proteins were immunoprecipitated and visualized as described elsewhere (20).

TDP-43S Protein Production. Mouse TDP-43 DNA was used to PCR base pairs corresponding to residues 101–265 and cloned into the pGEX3x expression vector. D169G and K263E mutations were generated from the wild-type mTDP-43S pGEX3x plasmid using site-directed mutagenesis. The mTDP-43S fusion protein, which contained a cleavable N-terminal GST protein tag was expressed in *Escherichia coli* BL21 (DE3) by induction with 1.0 mM Isopropyl β-D-1-thiogalactopyranoside and cultured at 30 °C for 5 h. The GST-mTDP-43S protein was purified on a glutathione Sepharose column equilibrated with 50 mM Tris·HCl pH 7.4, 150 mM NaCl, 2 mM $CaCl_2$. A 500-mM NaCl wash in the same buffer was performed on-column to remove any DNA or RNA bound to GST-TDP-43S. GST was cleaved on-column with addition of Factor Xa and incubation overnight at 4 °C. Factor Xa was removed by elution through a benzamidine column. Size exclusion chromatography was performed on a Superdex 200 16/600 or Superdex 75 10/300. DNA binding was achieved by addition of equimolar amounts of TG repeat oligonucleotides.

TDP-43S Unfolding Experiments. The temperature dependence of Sypro-orange (10×) fluorescence in the presence of TDP-43S variants (25 μM) was measured over a temperature range of 14–95 °C, increasing at a rate of 1.2 °C/min. Fluorescence was measured at ~470 nm and ~610 nm for excitation and emission, respectively. A total of 8 melt curves for wild-type, K263E, and D169G constructs with 4×, 8×, and 16× TG repeat DNA were obtained and averaged and their first derivatives calculated to obtain the melting temperatures.

Aromatic fluorescence of the samples was tested at a concentration of 0.45 mg/mL using excitation and emission wavelengths of 280 nm and 340 nm, respectively. A total of six repeats for each variant and buffer were performed. Samples and buffer were preheated for 5 min over 2 °C increments from 37 to 65 °C. The samples were buffer subtracted and averaged to produce the data points and SD. Boltzmann curve fitting was calculated using Origin 8.6 (OriginLab).

SAXS Data Collection, Processing, and Interpretation. SAXS data collection for modeling purposes was performed at beamline SWING (58) at Synchrotron Soleil, which is suited to the characterization of aggregation prone proteins (45). Concentrated TDP-43S (40 μL, 5–10 mg/mL) was separated from high molecular weight aggregates on a Shodex KW402.5–4F SEC column with 300 μL/min flow. A total of 250 exposures spanning the protein elution were collected on an Aviex 170 × 170 charged coupled detector, over an angular momentum transfer range (q) of 0.01–0.57, where $q = 4\pi\sin\theta\lambda^{-1}$ (λ is the wavelength of the incident radiation and θ is half the angle between the incident and scattered radiation). Data averaging, reduction, and preliminary Rg and I(0) calculations were performed using FoxTrot software, developed in-house at Soleil, but scrutinized in more detail with PRIMUS (59). Distance distribution functions P(r) were calculated with Gnom (60). Ten-bead models, generated with GASBOR (61), were averaged using DAMAVER to yield an average electron density model. Rigid body refinement using human RRM1 [Protein Data Bank (PDB): 2CQG, residues 106–177] and mouse RRM2 (PDB: 3D2W, residues 193–259) was performed against experimental SAXS data using BUNCH (62). Residues including N-terminal Gly, Ile and Leu (remaining after factor Xa cleavage) and 101–105, 178–192 and 260–265 were modelled from the Cα trace and reconstituted using SABBAC (63). Rigid-body and bead models were visualized and aligned with PyMOL (www.pymol.org). All curve fittings and 1D profile estimations mentioned were performed using CRYSOL (64). Molecular weight estimations were determined using SAXS MoW (46).

Radii of gyration at 20 °C and 40 °C were calculated by the Guinier approximation using data collected at the Barkla X-ray Laboratory of Biophysics at the University of Liverpool (65). TDP-43S samples were concentrated to 3 mg/mL in the buffer previously described but with the addition of 20 mM DTT. Scattering was collected on a MAR300 image plate at a distance of 1.25 m from the sample. Protein and buffer scattering was recorded over three separate 20-min exposures, which were then averaged. Data integration and analysis was performed using Fit2D and PRIMUS. The bounds of the Guinier region (qRg) all lay below 1.3 for each construct except the wild type at 40 °C, which, due to extensive aggregation, was 2.0.

Circular Dichroism. The optical activity of TDP-43S variants was determined at beamline DISCO also at Synchrotron Soleil. Following dialysis against 50 mM phosphate buffer pH 7.2, 50 mM NaF and concentration to 0.8 mg/mL, measurements were taken using a 0.02-cm quartz cell and 9-s acquisition time in range 180–260 nm. Data acquisition was repeated three times for each construct before buffer subtraction, averaging, and smoothing by averaging two consecutive points. CDSSTR secondary structure prediction was performed using the DichroWeb on-line server, using the SP175 reference set.

ACKNOWLEDGMENTS. We acknowledge the interest and help of Prof. Bob Eady, Dr. Richard Strange, and Dr. Hyun Chul Lee. We are grateful to the staff of SWING and DISCO beamlines at Synchrotron SOLEIL for provision of SAXS and CD facilities and their helpful guidance. This work was funded by the Motor Neurone Disease Association (Grant Hasnain/Apr11/6076 to S.S.H. and S.V.A.); the Science and Technologies Funding Council (J.G.G. and S.S.H.); the University of Liverpool, Grants-in-Aid for Scientific Research [Grants 23111006 (to K.Y.) and 22700404 (to S.W.)]; the Ministry for Education, Culture and Sports, Science, and Technology of Japan; the Research Committee of CNS Degenerative Diseases, the Ministry of Health, Labour, and Welfare of Japan; and Japan Science Technology, CREST. Access to SOLEIL was partly funded by the European Community's Seventh Framework Programme (FP7/2007-2013) under BioStruct-X (Grant Agreement 283570 and Proposal 2370).

1. Koo EH, Lansbury PT, Jr., Kelly JW (1999) Amyloid diseases: Abnormal protein aggregation in neurodegeneration. *Proc Natl Acad Sci USA* 96(18):9989–9990.
2. Hough MA, et al. (2004) Dimer destabilization in superoxide dismutase may result in disease-causing properties: Structures of motor neuron disease mutants. *Proc Natl Acad Sci USA* 101(16):5976–5981.
3. Bruijn LI, et al. (1998) Aggregation and motor neuron toxicity of an ALS-linked SOD1 mutant independent from wild-type SOD1. *Science* 281(5384):1851–1854.
4. Wang Q, Johnson JL, Agar NYR, Agar JN (2008) Protein aggregation and protein instability govern familial amyotrophic lateral sclerosis patient survival. *PLoS Biol* 6(7):e170.
5. Sreedharan J, et al. (2008) TDP-43 mutations in familial and sporadic amyotrophic lateral sclerosis. *Science* 319(5870):1668–1672.
6. Kabashi E, et al. (2008) TARDBP mutations in individuals with sporadic and familial amyotrophic lateral sclerosis. *Nat Genet* 40(5):572–574.
7. Neumann M, et al. (2006) Ubiquitinated TDP-43 in frontotemporal lobar degeneration and amyotrophic lateral sclerosis. *Science* 314(5796):130–133.
8. Higashi S, et al. (2007) Concurrence of TDP-43, tau and alpha-synuclein pathology in brains of Alzheimer's disease and dementia with Lewy bodies. *Brain Res* 1184: 284–294.
9. Hasegawa M, et al. (2007) TDP-43 is deposited in the Guam parkinsonism-dementia complex brains. *Brain* 130(Pt 5):1386–1394.
10. Ou SH, Wu F, Harrich D, García-Martínez LF, Gaynor RB (1995) Cloning and characterization of a novel cellular protein, TDP-43, that binds to human immunodeficiency virus type 1 TAR DNA sequence motifs. *J Virol* 69(6):3584–3596.
11. Fallini C, Bassell GJ, Rossoll W (2012) The ALS disease protein TDP-43 is actively transported in motor neuron axons and regulates axon outgrowth. *Hum Mol Genet* 21(16):3703–3718.
12. Colombrita C, et al. (2009) TDP-43 is recruited to stress granules in conditions of oxidative insult. *J Neurochem* 111(4):1051–1061.
13. Wang I-F, Wu L-S, Chang H-Y, Shen C-KJ (2008) TDP-43, the signature protein of FTLD-U, is a neuronal activity-responsive factor. *J Neurochem* 105(3):797–806.
14. Buratti E, et al. (2001) Nuclear factor TDP-43 and SR proteins promote in vitro and in vivo CFTR exon 9 skipping. *EMBO J* 20(7):1774–1784.
15. Ayala YM, et al. (2011) TDP-43 regulates its mRNA levels through a negative feedback loop. *EMBO J* 30(2):277–288.
16. Polymenidou M, et al. (2011) Long pre-mRNA depletion and RNA missplicing contribute to neuronal vulnerability from loss of TDP-43. *Nat Neurosci* 14(4):459–468.
17. Tollervey JR, et al. (2011) Characterizing the RNA targets and position-dependent splicing regulation by TDP-43. *Nat Neurosci* 14(4):452–458.
18. Iguchi Y, et al. (2013) Loss of TDP-43 causes age-dependent progressive motor neuron degeneration. *Brain* 136(Pt 5):1371–1382.
19. Wils H, et al. (2010) TDP-43 transgenic mice develop spastic paralysis and neuronal inclusions characteristic of ALS and frontotemporal lobar degeneration. *Proc Natl Acad Sci USA* 107(8):3858–3863.
20. Watanabe S, Kaneko K, Yamanaka K (2013) Accelerated disease onset with stabilized familial amyotrophic lateral sclerosis (ALS)-linked mutant TDP-43 proteins. *J Biol Chem* 288(5):3641–3654.
21. Ling S-C, et al. (2010) ALS-associated mutations in TDP-43 increase its stability and promote TDP-43 complexes with FUS/TLS. *Proc Natl Acad Sci USA* 107(30): 13318–13323.
22. Bhardwaj A, Myers MP, Buratti E, Baralle FE (2013) Characterizing TDP-43 interaction with its RNA targets. *Nucleic Acids Res* 41(9):5062–5074.
23. Liu X, et al. (2013) The RRM domain of human fused in sarcoma protein reveals a non-canonical nucleic acid binding site. *Biochim Biophys Acta* 1832(2):375–385.
24. Kuo P-H, Doudeva LG, Wang Y-T, Shen C-KJ, Yuan HS (2009) Structural insights into TDP-43 in nucleic-acid binding and domain interactions. *Nucleic Acids Res* 37(6): 1799–1808.
25. Tsuiji H, et al. (2013) Spliceosome integrity is defective in the motor neuron diseases ALS and SMA. *EMBO Mol Med* 5(2):221–234.
26. Wang Y-T, et al. (2013) The truncated C-terminal RNA recognition motif of TDP-43 protein plays a key role in forming proteinaceous aggregates. *J Biol Chem* 288(13): 9049–9057.
27. Guo W, et al. (2011) An ALS-associated mutation affecting TDP-43 enhances protein aggregation, fibril formation and neurotoxicity. *Nat Struct Mol Biol* 18(7):822–830.
28. Johnson BS, McCaffery JM, Lindquist S, Gitler AD (2008) A yeast TDP-43 proteinopathy model: Exploring the molecular determinants of TDP-43 aggregation and cellular toxicity. *Proc Natl Acad Sci USA* 105(17):6439–6444.
29. Ihara R, et al. (2013) RNA binding mediates neurotoxicity in the transgenic Drosophila model of TDP-43 proteinopathy. *Hum Mol Genet* 22(22):4474–4484.
30. Bentmann E, et al. (2012) Requirements for stress granule recruitment of fused in sarcoma (FUS) and TAR DNA-binding protein of 43 kDa (TDP-43). *J Biol Chem* 287(27): 23079–23094.
31. McDonald KK, et al. (2011) TAR DNA-binding protein 43 (TDP-43) regulates stress granule dynamics via differential regulation of G3BP and TIA-1. *Hum Mol Genet* 20(7):1400–1410.
32. Kovacs GG, et al. (2009) TARDBP variation associated with frontotemporal dementia, supranuclear gaze palsy, and chorea. *Mov Disord* 24(12):1843–1847.
33. Lukavsky PJ, et al. (2013) Molecular basis of UG-rich RNA recognition by the human splicing factor TDP-43. *Nat Struct Mol Biol* 20(12):1443–1449.
34. Soto C (2003) Unfolding the role of protein misfolding in neurodegenerative diseases. *Nat Rev Neurosci* 4(1):49–60.
35. Chang CK, et al. (2012) The N-terminus of TDP-43 promotes its oligomerization and enhances DNA binding affinity. *Biochem Biophys Res Commun* 425(2):219–224.
36. Tam S, et al. (2009) The chaperonin TRiC blocks a huntingtin sequence element that promotes the conformational switch to aggregation. *Nat Struct Mol Biol* 16(12): 1279–1285.
37. Vassall KA, et al. (2011) Decreased stability and increased formation of soluble aggregates by immature superoxide dismutase do not account for disease severity in ALS. *Proc Natl Acad Sci USA* 108(6):2210–2215.
38. Andersson FI, et al. (2011) The effect of Parkinson's-disease-associated mutations on the deubiquitinating enzyme UCH-L1. *J Mol Biol* 407(2):261–272.
39. Ni C-L, Shi H-P, Yu H-M, Chang Y-C, Chen Y-R (2011) Folding stability of amyloid-beta 40 monomer is an important determinant of the nucleation kinetics in fibrillization. *FASEB J* 25(4):1390–1401.
40. Münch C, Bertolotti A (2010) Exposure of hydrophobic surfaces initiates aggregation of diverse ALS-causing superoxide dismutase-1 mutants. *J Mol Biol* 399(3):512–525.
41. Niesen FH, Berglund H, Vedadi M (2007) The use of differential scanning fluorimetry to detect ligand interactions that promote protein stability. *Nat Protoc* 2(9):2212–2221.
42. Eftink MR (1994) The use of fluorescence methods to monitor unfolding transitions in proteins. *Biophys J* 66(2 Pt 1):482–501.
43. Jacques DA, Trewhella J (2010) Small-angle scattering for structural biology—expanding the frontier while avoiding the pitfalls. *Protein Sci* 19(4):642–657.
44. Wright GSA, Antonyuk SV, Kershaw NM, Strange RW, Samar Hasnain S (2013) Ligand binding and aggregation of pathogenic SOD1. *Nat Commun* 4:1758.
45. Wright GSA, Hasnain SS, Grossmann JG (2011) The structural plasticity of the human copper chaperone for SOD1: Insights from combined size-exclusion chromatographic and solution X-ray scattering studies. *Biochem J* 439(1):39–44.
46. Fischer H, de Oliveira Neto M, Napolitano HB, Polikarpov I, Craievich AF (2009) Determination of the molecular weight of proteins in solution from a single small-angle X-ray scattering measurement on a relative scale. *J Appl Cryst* 43:101–109.
47. Chen-Plotkin AS, Lee VM-Y, Trojanowski JQ (2010) TAR DNA-binding protein 43 in neurodegenerative disease. *Nat Rev Neurol* 6(4):211–220.
48. McLendon G, Radany E (1978) Is protein turnover thermodynamically controlled? *J Biol Chem* 253(18):6335–6337.
49. Inoue I, Rechsteiner M (1994) On the relationship between the metabolic and thermodynamic stabilities of T4 lysozymes. Measurements in eukaryotic cells. *J Biol Chem* 269(46):29247–29251.
50. Parsell DA, Sauer RT (1989) The structural stability of a protein is an important determinant of its proteolytic susceptibility in Escherichia coli. *J Biol Chem* 264(13): 7590–7595.
51. Hasegawa M, et al. (2008) Phosphorylated TDP-43 in frontotemporal lobar degeneration and amyotrophic lateral sclerosis. *Ann Neurol* 64(1):60–70.
52. Zhang Y-J, et al. (2009) Aberrant cleavage of TDP-43 enhances aggregation and cellular toxicity. *Proc Natl Acad Sci USA* 106(18):7607–7612.
53. Arai T, et al. (2010) Phosphorylated and cleaved TDP-43 in ALS, FTLD and other neurodegenerative disorders and in cellular models of TDP-43 proteinopathy. *Neuropathology* 30(2):170–181.
54. Arnold ES, et al. (2013) ALS-linked TDP-43 mutations produce aberrant RNA splicing and adult-onset motor neuron disease without aggregation or loss of nuclear TDP-43. *Proc Natl Acad Sci USA* 110(8):E736–E745.
55. Liu R, et al. (2013) Reducing TDP-43 aggregation does not prevent its cytotoxicity. *Acta Neuropathol Commun* 1(1):49.
56. Zhang Y-J, et al. (2010) Phosphorylation regulates proteasomal-mediated degradation and solubility of TAR DNA binding protein-43 C-terminal fragments. *Mol Neurodegener* 5:33.
57. Ross CA, Poirier MA (2004) Protein aggregation and neurodegenerative disease. *Nat Med* 10(Suppl):S10–S17.
58. David G, Pérez J (2009) Combined sampler robot and high-performance liquid chromatography: A fully automated system for biological small-angle X-ray scattering experiments at the Synchrotron SOLEIL SWING beamline. *J Appl Cryst* 42:892–900.
59. Konarev PV, Volkov VV, Sokolova AV, Koch MHJ, Svergun DI (2003) *PRIMUS*: A Windows PC-based system for small-angle scattering data analysis. *J Appl Cryst* 36: 1277–1282.
60. Svergun DI (1992) Determination of the regularization parameter in indirect-transform methods using perceptual criteria. *J Appl Cryst* 25:495–503.
61. Svergun DI, Petoukhov MV, Koch MH (2001) Determination of domain structure of proteins from X-ray solution scattering. *Biophys J* 80(6):2946–2953.
62. Petoukhov MV, Svergun DI (2005) Global rigid body modeling of macromolecular complexes against small-angle scattering data. *Biophys J* 89(2):1237–1250.
63. Maupetit J, Gautier R, Tufféry P (2006) SABBAC: Online structural alphabet-based protein backbone reconstruction from alpha-carbon trace. *Nucleic Acids Res* 34(Web Server issue):W147–151.
64. Svergun D, Barberato C, Koch MHJ (1995) *CRYSOL*: A program to evaluate x-ray solution scattering of biological macromolecules from atomic coordinates. *J Appl Cryst* 28:768–773.
65. Wright GSA, et al. (2013) The application of hybrid pixel detectors for in-house SAXS instrumentation with a view to combined chromatographic operation. *J Synchrotron Radiat* 20(Pt 2):383–385.